

AD-A258 592

(19)



The Pennsylvania State University
APPLIED RESEARCH LABORATORY
P.O. Box 30
State College, PA 16804

DTIC
ELECTE
DEC 1 1992
S C D

DIGITAL IMAGE PROCESSING OF HYDROGEN
BUBBLE LINES FOR INSTANTANEOUS
VELOCITY PROFILES

by

S. D. Bruneau
W. R. Pauley

Technical Report No. TR 92-10
November 1992

Supported by:
Office of Chief of Naval Research

L.R. Hettche, Director
Applied Research Laboratory

Approved for public release; distribution unlimited

92-30512



11480

REPORT DOCUMENTATION PAGEForm Approved
OMB No. 0704-0188

Public reporting burden for this collection of information is estimated to average 1 hour per response, including the time for reviewing instructions, searching existing data sources, gathering and maintaining the data needed, and completing and reviewing the collection of information. Send comments regarding this burden estimate or any other aspect of this collection of information, including suggestions for reducing this burden, to Washington Headquarters Services, Directorate for Information Operations and Reports, 1215 Jefferson Davis Highway, Suite 1204, Arlington, VA 22202-4302, and to the Office of Management and Budget, Paperwork Reduction Project (0704-0188), Washington, DC 20503.

1. AGENCY USE ONLY (Leave blank)		2. REPORT DATE November 1992	3. REPORT TYPE AND DATES COVERED	
4. TITLE AND SUBTITLE Digital Image Processing of Hydrogen Bubble Lines for Instantaneous Velocity Profiles			5. FUNDING NUMBERS N00014-90-J-1365	
6. AUTHOR(S) S. D. Bruneau, W. R. Pauley				
7. PERFORMING ORGANIZATION NAME(S) AND ADDRESS(ES) Applied Research Laboratory The Pennsylvania State University P.O. Box 30 State College, PA 16804			8. PERFORMING ORGANIZATION REPORT NUMBER TR#92-10	
9. SPONSORING / MONITORING AGENCY NAME(S) AND ADDRESS(ES) Office of Chief of Naval Research Department of the Navy 800 North Quincy Street Arlington, VA 22217-5000			10. SPONSORING / MONITORING AGENCY REPORT NUMBER	
11. SUPPLEMENTARY NOTES				
12a. DISTRIBUTION / AVAILABILITY STATEMENT Unlimited			12b. DISTRIBUTION CODE	
13. ABSTRACT (Maximum 200 words) Boundary layer transition and turbulence have been described as being comprised of smaller structures called turbulent spots. Many researchers have obtained ensemble averaged velocity measurements in the transition region and some attempts have been made to obtain instantaneous information. Ensemble averaging can predict the overall scales of the flow field but it fails to yield information on the flow physics of the substructures within the spot. To facilitate investigation of these flow features and to establish the spot's relationship with transition or turbulence, an experimental method to obtain instantaneous full velocity profiles has been developed. The qualitative hydrogen bubble technique of flow visualization has been augmented to yield quantitative unsteady boundary layer information. The technique has been advanced by incorporating digital image processing of videotaped boundary layer flow. The method was verified by direct comparison with a laser Doppler anemometer and an analytical uncertainty analysis was performed. The technique compared well against the LDA in both steady and unsteady flows. Recommendations were made for effective use of this technique and for further development.				
14. SUBJECT TERMS velocity profiles, turbulent spots, experimental method, hydrogen bubble, flow visualization			15. NUMBER OF PAGES 104	
			16. PRICE CODE	
17. SECURITY CLASSIFICATION OF REPORT UNCLASSIFIED	18. SECURITY CLASSIFICATION OF THIS PAGE UNCLASSIFIED	19. SECURITY CLASSIFICATION OF ABSTRACT UNCLASSIFIED	20. LIMITATION OF ABSTRACT UNLIMITED	

GENERAL INSTRUCTIONS FOR COMPLETING SF 298

The Report Documentation Page (RDP) is used in announcing and cataloging reports. It is important that this information be consistent with the rest of the report, particularly the cover and title page. Instructions for filling in each block of the form follow. It is important to *stay within the lines* to meet optical scanning requirements.

Block 1. Agency Use Only (Leave blank).

Block 2. Report Date. Full publication date including day, month, and year, if available (e.g. 1 Jan 88). Must cite at least the year.

Block 3. Type of Report and Dates Covered. State whether report is interim, final, etc. If applicable, enter inclusive report dates (e.g. 10 Jun 87 - 30 Jun 88).

Block 4. Title and Subtitle. A title is taken from the part of the report that provides the most meaningful and complete information. When a report is prepared in more than one volume, repeat the primary title, add volume number, and include subtitle for the specific volume. On classified documents enter the title classification in parentheses.

Block 5. Funding Numbers. To include contract and grant numbers; may include program element number(s), project number(s), task number(s), and work unit number(s). Use the following labels:

C - Contract	PR - Project
G - Grant	TA - Task
PE - Program Element	WU - Work Unit Accession No.

Block 6. Author(s). Name(s) of person(s) responsible for writing the report, performing the research, or credited with the content of the report. If editor or compiler, this should follow the name(s).

Block 7. Performing Organization Name(s) and Address(es). Self-explanatory.

Block 8. Performing Organization Report Number. Enter the unique alphanumeric report number(s) assigned by the organization performing the report.

Block 9. Sponsoring/Monitoring Agency Name(s) and Address(es). Self-explanatory.

Block 10. Sponsoring/Monitoring Agency Report Number. (If known)

Block 11. Supplementary Notes. Enter information not included elsewhere such as: Prepared in cooperation with...; Trans. of...; To be published in.... When a report is revised, include a statement whether the new report supersedes or supplements the older report.

Block 12a. Distribution/Availability Statement. Denotes public availability or limitations. Cite any availability to the public. Enter additional limitations or special markings in all capitals (e.g. NOFORN, REL, ITAR).

DOD - See DoDD 5230.24, "Distribution Statements on Technical Documents."

DOE - See authorities.

NASA - See Handbook NHB 2200.2.

NTIS - Leave blank.

Block 12b. Distribution Code.

DOD - Leave blank.

DOE - Enter DOE distribution categories from the Standard Distribution for Unclassified Scientific and Technical Reports.

NASA - Leave blank.

NTIS - Leave blank.

Block 13. Abstract. Include a brief (*Maximum 200 words*) factual summary of the most significant information contained in the report.

Block 14. Subject Terms. Keywords or phrases identifying major subjects in the report.

Block 15. Number of Pages. Enter the total number of pages.

Block 16. Price Code. Enter appropriate price code (*NTIS only*).

Blocks 17. - 19. Security Classifications. Self-explanatory. Enter U.S. Security Classification in accordance with U.S. Security Regulations (i.e., UNCLASSIFIED). If form contains classified information, stamp classification on the top and bottom of the page.

Block 20. Limitation of Abstract. This block must be completed to assign a limitation to the abstract. Enter either UL (unlimited) or SAR (same as report). An entry in this block is necessary if the abstract is to be limited. If blank, the abstract is assumed to be unlimited.

ABSTRACT

Boundary layer transition and turbulence have been described as being comprised of smaller structures called turbulent spots. Many researchers have obtained ensemble averaged velocity measurements in the transition region and some attempts have been made to obtain instantaneous information. Ensemble averaging can predict the overall scales of the flow field but it fails to yield information on the flow physics of the substructures within the spot. To facilitate investigation of these flow features and to establish the spot's relationship with transition or turbulence, an experimental method to obtain instantaneous full velocity profiles has been developed. The qualitative hydrogen bubble technique of flow visualization has been augmented to yield quantitative unsteady boundary layer information. The technique has been advanced by incorporating digital image processing of videotaped boundary layer flow. The method was verified by direct comparison with a laser Doppler anemometer and an analytical uncertainty analysis was performed. The technique compared well against the LDA in both steady and unsteady flows. Recommendations were made for effective use of this technique and for further development.

Accession For	
NTIS 02101	<input checked="" type="checkbox"/>
DTIC TAB	<input type="checkbox"/>
Unannounced	<input type="checkbox"/>
Justification	
By _____	
Distribution/	
Availability Codes	
Dist	Avail and/or Special
A-1	

TABLE OF CONTENTS**LIST OF FIGURES**

vi

CHAPTER 1. INTRODUCTION	1
1.1. Problem Statement	1
1.2. Unsteady Flow/ Turbulent Spots	3
1.3. Hydrogen Bubble Technique	7
1.4. The Electrolysis of Water	9
1.5. Sources of Error	11
CHAPTER 2. FACILITY	15
2.1. Laminar Flow Open Surface Water Channel	15
2.2. Hydrogen Bubble Apparatus	18
2.2.1. Design Specifications	18
2.2.2. Apparatus Design	20
2.2.2.1 Video Camera Trigger	20
2.2.2.2 Signal Conditioning	22
2.2.2.3 DAS-16 and DC Power	25
2.2.2.4 Experimental Setup	28
2.3. Digital Image Processing	31
2.3.1. Processing System Overview	31

	v
2.3.2. Still Image/Time Base Correction	33
2.3.3. Image Processing Procedure	34
CHAPTER 3. RESULTS AND DISCUSSION	42
3.1. Falkner Skan Velocity Profile Test	43
3.2. Analytical Uncertainty Analysis	45
3.3. Hydrogen Bubble vs. LDA (Laminar)	57
3.4. Hydrogen Bubble vs. LDA (Turbulent Spots)	80
CHAPTER 4. CONCLUSIONS AND RECOMMENDATIONS	98
4.1. Conclusions of Present Study	98
4.2. Recommendations and Future Considerations	99
REFERENCES	102

LIST OF FIGURES

1.	The Turbulent Spot Characteristics; a) in Plan View, b) and Side View	5
2.	Aerospace Engineering Laminar Flow Water Channel	16
3.	Hydrogen Bubble System Flow Chart	21
4.	Composite Video Signal-Negative Sync	24
5.	Video Signal Conditioning	26
6.	Signal Conditioning Circuit Diagram	27
7.	Bubble Wire Holder	29
8.	Experimental Lighting Configuration	30
9.	Edge Detection Scheme	36
10.	Coefficient Masks for Image Processing	38
11.	Falkner Skan Actual and Processed	44
12.	Bubble Trajectory Analysis Case 1	52
13.	Bubble Trajectory Analysis Case 2	54
14.	Bubble Trajectory Analysis Case 3	55
15.	Bubble Trajectory Analysis Case 4	56
16.	Instantaneous Hydrogen Bubble vs. LDA (15 cm/s, $t = 1/30$ sec)	61
17.	Instantaneous Hydrogen Bubble vs. LDA (18.9 cm/s, $t = 1/30$ sec)	62
18.	Instantaneous Hydrogen Bubble vs. LDA (22.22 cm/s, $t=1/30$ sec)	63
19.	Instantaneous Hydrogen Bubble vs. LDA (15 cm/s, $t = 1/15$ sec)	64
20.	Instantaneous Hydrogen Bubble vs. LDA (18.9 cm/s, $t=1/15$ sec)	65

21.	Instantaneous Hydrogen Bubble vs. LDA (22.22 cm/s,t=1/15 sec)	66
22.	Time-Averaged Hydrogen Bubble vs. LDA (15 cm/s,t=1/30 sec)	68
23.	Time-Averaged Hydrogen Bubble vs. LDA (18.9 cm/s,t=1/30 sec)	69
24.	Time-Averaged Hydrogen Bubble vs. LDA (22.22 cm/s, t=1/30 sec)	70
25.	Time-Averaged Hydrogen Bubble vs. LDA (15 cm/s,t = 1/15 sec)	71
26.	Time-Averaged Hydrogen Bubble vs. LDA (18.9 cm/s,t = 1/15 sec)	72
27.	Time-Averaged Hydrogen Bubble vs. LDA (22.22 cm/s,t = 1/15 sec)	73
28.	Hydrogen Bubble Integral Parameters vs. Time (15cm/s,t = 1/30 sec)	74
29.	Hydrogen Bubble Integral Parameters vs. Time (18.9 cm/s,t = 1/30 sec)	75
30.	Hydrogen Bubble Integral Parameters vs. Time (22.22 cm/s,t=1/30 sec)	76
31.	Hydrogen Bubble Integral Parameters vs. Time (15 cm/s, t=1/15 sec)	77
32.	Hydrogen Bubble Integral Parameters vs. Time (18.9 cm/s,t = 1/15 sec)	78
33.	Hydrogen Bubble Integral Parameters vs. Time (22.22 cm/s,t=1/15 sec)	79
34.	The Effects on the Velocity Profile by Shifting the Wall Pixel by Two	81
35.	Ensemble-Averaged δ^* vs. Time for Hydrogen Bubble and LDA	84
36.	Hydrogen Bubble and LDA Ensemble-Averaged Velocity Profiles at t = 7.6 seconds.	85
37.	Hydrogen Bubble and LDA Ensemble-Averaged Velocity Profiles at t = 9.75 seconds.	86

38.	Actual Video Frames from Turbulent Spot Passing: a) Laminar Flow Timelines for Comparison with times at b) 7.53334 c) 7.56667 d) 7.600 e) 7.63333 f) Processed Image at 7.63333 sec.	87
39.	Actual Video Frames from Turbulent Spot Passing: a) Laminar Flow Timelines for Comparison with times at b) 9.73332 c) 9.76665 d) 9.79998 e) 9.83331 f) Processed Image at 9.83331 sec.	88
40.	Hydrogen Bubble Instantaneous δ^* vs. Time Spot #1.	90
41.	Hydrogen Bubble Instantaneous δ^* vs. Time Spot #5.	91
42.	Hydrogen Bubble Instantaneous δ^* vs. Time Spot #10.	92
43.	Hydrogen Bubble Instantaneous δ^* vs. Time Spot #15.	93
44.	Hydrogen Bubble Instantaneous δ^* vs. Time Spot #20.	94
45.	Hydrogen Bubble Instantaneous δ^* vs. Time Spot #25	95
46.	Hydrogen Bubble Instantaneous δ^* vs. Time Spot #30.	96

CHAPTER 1

INTRODUCTION

1.1. Problem Statement

There are several techniques commonly used to measure instantaneous flow velocity, such as hot wire and hot film anemometry, and laser Doppler anemometry. While they are effective in making single point measurements, they are not capable of measuring information at many locations simultaneously. To obtain descriptions of full flowfields with traditional techniques, measurements must be made at a single location and then the measurement system must be traversed using either manual or automated positioning hardware to subsequent locations. This procedure results in an averaged description of the flow. A major limitation of either hot wires or hot films is that they are an intrusive method and can disrupt the flow. Velocity fields as well as pressure distributions are changed significantly by the presence of these instruments. In order to obtain instantaneous velocity information at several locations, a rake comprised of multiple hot wires or hot films can be used. Rakes, or groups, of hot wires/hot films, result in significant flow disturbance and are complex to operate due to the requirement that each probe have its own electrical bridge.

Hot wires and hot films have been successfully used in water, but they must be used with extreme caution. In water the hot wire forms small air bubbles on and around the wire and dust particles in the flow adhere to it (Hatanu and Hotta, 1983). Hot films exhibit similar problems along with the additional complication of boiling

and electrolysis at the probe. Contaminants on the film result in a change in the heat transfer between the sensor and the water which causes drift in the anemometer calibration. Electrolysis is a serious problem because it erodes the hot film or hot wire (Rasmussen, 1967).

Laser Doppler Anemometry (LDA) is non-intrusive but is limited because it cannot always yield instantaneous velocities "on demand." It is dependent on the data rate which is determined by the laser power and seeding density. Even with very high seed density which produces nearly "instantaneous" signals, measuring the entire flowfield to obtain ensemble averages of unsteady events requires considerable time between samples. Because of the difficulties inherent in these methods, they are inadequate for measuring instantaneous complete velocity profile information.

The objective of this project is to develop automated processing of hydrogen bubble timelines produced by the electrolysis of water at a wire placed normal to a test surface. Records of the resulting bubble lines yield the instantaneous full velocity field information needed to describe the unsteady flowfield, $u(y,t)$. The hydrogen bubble method overcomes many of the limitations inherent in the other systems if the diameter of the wire is sufficiently small so that it does not disturb the flow. With an appropriate wire placement, complete instantaneous flow velocity information can be obtained by tracking bubbles through the region of interest.

Tracking hydrogen bubble paths has been used extensively in the past, along with traditional photography. The focus of this study is to develop an automated digital image processing procedure to convert the video pictures to useful velocity

information. We have developed this procedure for use in a water channel to measure instantaneous velocity profile information for steady and unsteady flow conditions. From this instantaneous velocity information, instantaneous estimates of the boundary layer scaler descriptions are obtained. In addition, the validity of the procedure is tested against a laser Doppler anemometer.

1.2. Unsteady Flow/Turbulent Spots

H. W. Emmons discovered in 1951 that transition to turbulence occurred through the appearance of small, individual patches of turbulence in an otherwise laminar boundary layer. He termed these patches spots and noted that they started at random locations and times. He noted that the spots grew and multiplied in the downstream direction until the spots coalesced into a fully turbulent boundary layer. From his findings, Emmons proposed that transition from laminar to turbulent flow occurs through the generation, growth, and amalgamation of turbulent spots (Riley and Gad-el-Hak, 1985). It has been suggested that spots are dynamically similar to turbulent boundary layers, and that turbulent boundary layers might be a composite of turbulent spots. Because of the possible links, the study of turbulent spots lends itself to the study of both boundary layer transition and turbulence (Riley and Gad-el-Hak 1985).

Many researchers have used fast response probes to study artificially initiated turbulent spots. From the work of researchers such as Schubauer and Klebanoff (1955), and Wygnanski et al. (1982), the general shape of the spot, its spread angle

and its propagation velocity have all been determined (figure 1). The lateral spread angle of a turbulent spot is typically 10° to each side of the plane of symmetry. In a plan view the spot has an arrowhead shape, with a leading interface convecting downstream at a speed of about 90 percent of the freestream velocity. The convection speed along the sides of the spot decreases to approximately 50 percent of the freestream (Riley and Gad-el-Hak, 1985). Immediately following the spot is a "calmed region" which is characterized by a full velocity profile which is more stable than the surrounding Blasius flow. The mean velocity profiles in the interior of the spot are similar to a turbulent boundary layer. The displacement thickness and momentum thickness change rapidly within the spot yet their ratio, the shape factor, remains relatively constant. The maximum height of the spot is approximately equal to the thickness of a hypothetical turbulent boundary layer. The height of the leading interface's overhang corresponds roughly to the thickness of the laminar boundary layer (Riley and Gad-el-Hak, 1985). Wygnanski et al. (1982) concluded that a similarity approach based on ensemble averaged data is severely limited in fully describing the turbulent spot. They noted that ensemble averaging might be used to predict the overall scales and flowfield, but a different approach must be taken to investigate the internal structures of the spot (Wygnanski et al. 1982).

There is evidence, mainly from flow visualization, that there exist several structures, possibly hairpinlike vortices, within a single spot. It has been observed that the number of structures increases as the spot convects downstream, accounting for the growth of the spot and the difference between convection velocities around

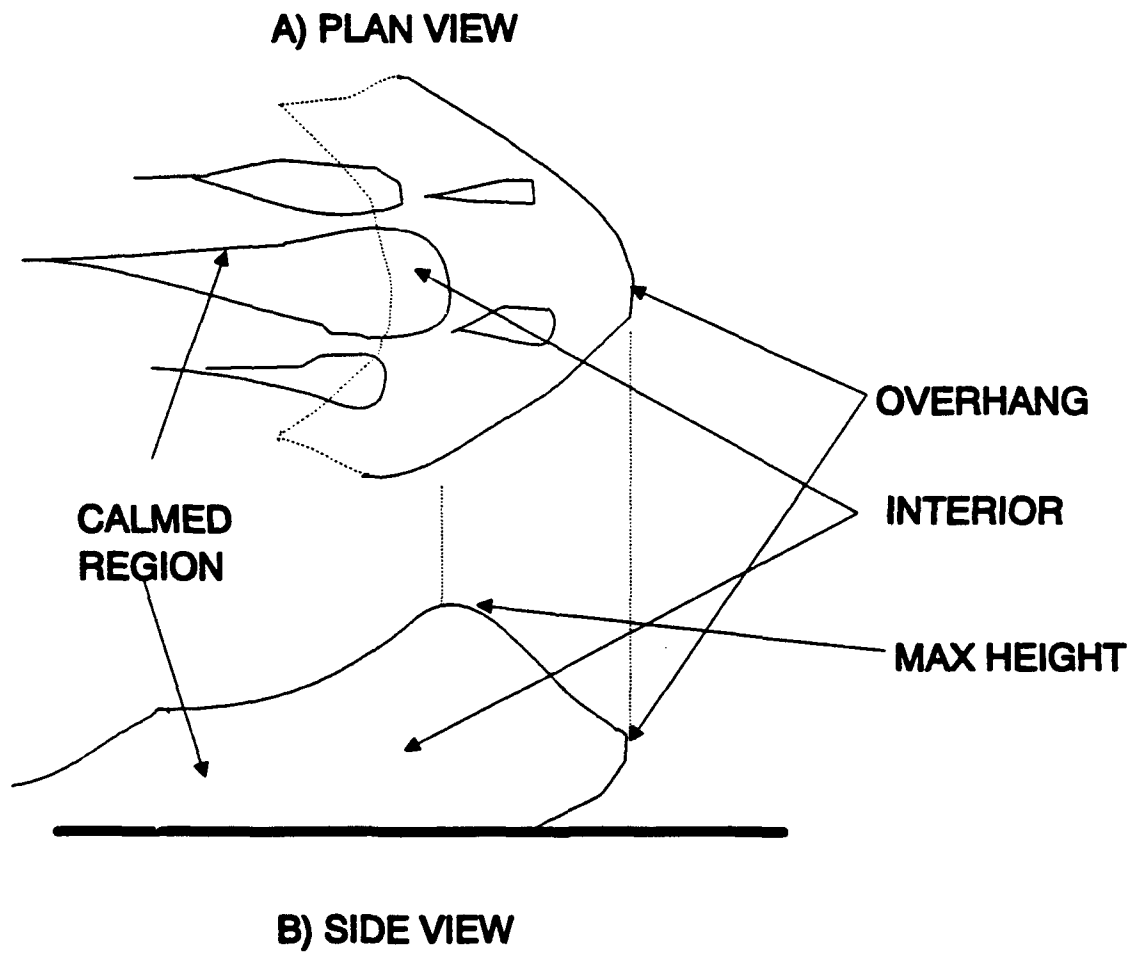


Figure 1. The Turbulent Spot Characteristics; a) in Plan View, b) and Side View.

the spot (Sankaran et al., 1991). Sankaran et al. (1991) suggest that due to the increased study and understanding of these internal structures, the idea that the transitional spot is the basic building block of the turbulent boundary layer should be reevaluated.

Sankaran et al. (1991) note that to obtain reliable quantitative information on the boundary layer flow structures, it is important to use experimental procedures which focus on the signatures of these structures. When the averaging is conditioned on either the trailing edge or leading edges of the spot, details associated with the internal structures are smeared. Ensemble averaging smears out all but the largest scales. Such averaged data lends itself well to the statistically descriptors such as arrival time and convection velocity. On the other hand, focusing on a single instantaneous realization of the spot provides useful insight into the flow physics, especially the evolution and dynamics of the spot (Sankaran et al., 1991). The smearing that occurs when ensemble averaging the passing of a turbulent spot is due to the fact that the internal structures vary in size, arrival time, and inclination from one spot to another. It is also due to the fact that the spots themselves vary in size and shape and contain varying numbers of structures (Sankaran et al., 1991).

The relationship of the turbulent spot to both transitional boundary layers and turbulence, as well as to noise generation, requires substantial research. Future research into the internal structures of the turbulent spot may be facilitated by the development of the automated hydrogen bubble method. The instantaneous measurements provided by the technique, properly verified, can be a useful tool for

the study of turbulent spots and their internal structures. The scope of this study is to develop and verify the accuracy of this hydrogen bubble wire method as a potential experimental tool for future research.

1.3. Hydrogen Bubble Technique

The hydrogen bubble technique actually came about by accident. F. X. Wortmann laid the foundation for the method by developing a technique for injecting tellurium into water by applying a current pulse to a wire (Davis and Fox, 1967). It was based on Faraday's Law concerning the dissolution of the electrode. E. W. Geller is credited with observing the evolution of gases as he tried to improve upon Wortmann's technique in his masters thesis in 1954. E. W. Geller is most recognized as the originator of the hydrogen bubble technique as we know it today. Further development of this technique was performed by D. W. Clutter and A. M. O. Smith at Douglas Aircraft Company. Clutter and Smith (1961) introduced the scientific world to the flexibility of the method. They demonstrated it in aerodynamic flows and internal flow systems, and recommended its use for studying flows in rivers, and even flows over mountains (Clutter and Smith, 1961).

The technique consists of using the bubbles produced by the electrolysis of water as a flow visualization tool. Using a fine wire mounted perpendicular to a wall as the cathode, or negative electrode, in a dc circuit, and another material such as brass, as the anode, or positive electrode, the production of hydrogen occurs on the wire when it is excited by an electric pulse. If the fine wire were made the anode,

oxygen bubbles would be produced. The wire is designated as the cathode because the hydrogen bubbles generated there are approximately half as large as oxygen bubbles produced there, and serve better as tracers of the flow due to their smaller buoyancy force. In a variation on the pulsing technique Clutter and Smith (1961) used an ac circuit, which caused the wire to oscillate between positive and negative charge, producing alternating "clouds" of oxygen and hydrogen. Single sign pulsing of a dc circuit, where the wire is always the negative electrode, was used exclusively in the present study.

By electrically pulsing the wire, hydrogen bubble "clouds" are formed and are then swept from the wire by the flow. This "cloud" then deforms to the shape of the local velocity profile $u(y,t)$. By pulsing the wire at a constant frequency, these "clouds" mark the flow at constant time intervals. These curves are known as timelines (Merzkirch, 1987).

Quantitative analysis of the hydrogen bubble lines was introduced by Schraub et al. (1965). They used the technique to measure time dependent velocity fields in low-speed water flows. Since Schraub et al. (1965), several others have utilized the technique to make quantitative measurements. Davis and Fox (1967) used hydrogen bubble wires in clear tubes, Kim et al. (1971) applied them in turbulent boundary layers, and Lu and Smith (1985) extended the technique to employ automated digital image processing in investigating turbulence statistics and bursting characteristics.

To derive velocity information from the timelines, video or photographic frames are analyzed. For each timeline, the local velocity is established using time-

of-flight techniques. The local bubble-line velocity at each y location is approximated as

$$u_b(y, t) = \frac{\Delta x}{\Delta t} \quad (1)$$

where Δx is the horizontal displacement between any two bubble time-lines and Δt is the period of time between bubble pulses. Applying this method to bubble trajectories at several locations, instantaneous velocity profiles can be obtained.

1.4. The Electrolysis of Water

The electrolysis of water produces gaseous hydrogen and oxygen. Faraday's Law states that if two electrodes are immersed in an aqueous solution of a salt, acid or base and connected to a source of continuous current of a sufficiently high tension, there will be a passage of electricity through the solution and at the same time various chemical reactions will occur at the electrodes. These reactions may include the evolution of gas, the separation of substances, the dissolution of the electrode, or the appearance of new substances in the solution (Milazzo 1963).

The "electric tension" is the electric potential difference, or voltage, between two points. This voltage is generated by an electrical field and is due to the passage of charge via a chemical reaction. In general, the passage of current through an electrode requires a voltage different from that which it would assume at equilibrium. Any voltage applied to an electrode in order to make a current pass through it

is called overvoltage. Milazzo points out that the passage of current occurs immediately after the voltage is applied and there is not even the smallest time interval between the application of the external voltage and the passage of current (Milazzo 1963).

As stated above, one of the chemical reactions which takes place is the evolution of gases. In the electrolysis of water, hydrogen is created at the cathode, the negative electrode, and oxygen is created at the anode. According to Faraday's Law each amperehour releases 0.037 g H₂ and 0.298 g O₂. These quantities by weight correspond to volumes of 0.4176 liters and 0.2088 liters respectively, at 0° C and 760 mm Hg.

Milazzo gives a summary of the important conditions that must be maintained to minimize the needed cell voltage in order to minimize energy consumption:

1. A judicious choice of electrode material to reduce energy losses due to overvoltage at that electrode, since some materials are superior for this process.
2. A higher temperature to lower the overvoltage and the specific resistance of the electrolyte.
3. Electrolyte concentration: a maximum specific conductance of the electrolyte can be achieved at a given temperature for a particular concentration.
4. Fast recirculation of the electrolyte aids in preventing the development of a concentration cell.

The more concentrated solution becomes diluted.

5. Any device aiding the prompt removal of the gas and vapor bubbles from between the electrodes allows the cross sectional area between the electrodes to be a maximum; the ohmic resistance is minimized.
6. The inner cell resistance can be reduced by keeping a suitable distance between the electrodes.
7. The inner cell resistance can be decreased by keeping the electrolyte in fast motion and by any constructive device which assists removal of the developing gas from the electrolyte.

1.5. Sources of Error

In the development of any method, the possible sources of error must be identified and evaluated. Schraub et al. (1965) estimated the error due to each potential source. Applying a method developed by Kline and McClintock (1953) to the velocity equation, eq. 1, the terms which yield a large uncertainty interval, and hence are the dominant contributors to the total uncertainty in the velocity, were singled out. Schraub et al. (1965) found that the potential error in the displacement scaling factor and the framing speed contributed less than one fifth of the total uncertainty in the Δx term. According to Schraub et al. (1965), Δx carries with it the greatest level of uncertainty (Schraub et al., 1965). Schraub gave seven factors

contributing to the uncertainty:

1. Measuring Δx on film
2. Averaging effects in changing velocity field
3. Possible displacement of the bubble out of the x-y plane of the generating wire
4. Response of the bubbles to fluctuations
5. Resolution problems due to finite bubble size and due to finite averaging intervals
6. Bubble rise due to buoyancy
7. Velocity defect behind the bubble generating wire.

Schraub et al. (1965) used manual techniques for measuring Δx . They noted that errors exist as a result of human error, friction in their film reader, optical distortions, film-image resolution limits, and so on. The averaging uncertainties arose from the use of a marker method, where one attempts to predict Eulerian velocity in the flow field at a point in time and space $u(x,y,z,t)$ by calculating the Lagrangian time average velocity of marker bubbles over a small time interval (Schraub et al. 1965). Lu and Smith (1985) assumed that the Eulerian velocity was equal to the Lagrangian time-line velocity because of the limited transit distance between bubble time-lines and the relatively short averaging time. Their results substantiated this assumption.

Displacement uncertainties due to the movement of bubbles out of the x-y

plane of the generating wire are dependent upon the flow characteristics. Schraub et al. (1965) point out that if spanwise displacements occur in a flow with large spanwise velocity gradients, then errors may be introduced into the estimates of Δx and u . Lu and Smith (1985) assumed that for small differential distances between bubble lines, the much smaller magnitudes of the v and w velocity components relative to u have a small influence on bubble line deformation.

Response uncertainties in Δx arise because the bubble does not respond instantaneously to changes in the fluid velocity surrounding it. According to Davis and Fox (1967) the bubble leaving the wire takes 0.1 ms to attain a velocity of 98 percent of the fluid velocity. It is a good approximation, therefore, to neglect this error source.

To deal with the wake effects of the wire, Lu and Smith (1985) utilized an equation for wake defect given by Abernathy et al. (1977) of the form,

$$\frac{(u - U_b)}{u} = C \left(\frac{x}{d} \right)^{-0.5} \quad (2)$$

where u is the true fluid velocity, U_b is the measured bubble velocity, x is the distance of the bubble from the generating wire, d is the wire diameter, and C is a coefficient which depends on both the local Reynolds number and the wire drag coefficient. Lu and Smith (1987) found $C=1.7$ to yield a reasonable fit of the data for their water channel facility for a wire diameter Reynolds Number of 3.65.

By taking into account the possible sources of error, the hydrogen bubble

method for obtaining instantaneous full velocity profile information is a very powerful tool. To further improve the method, automated digital image processing procedures are utilized.

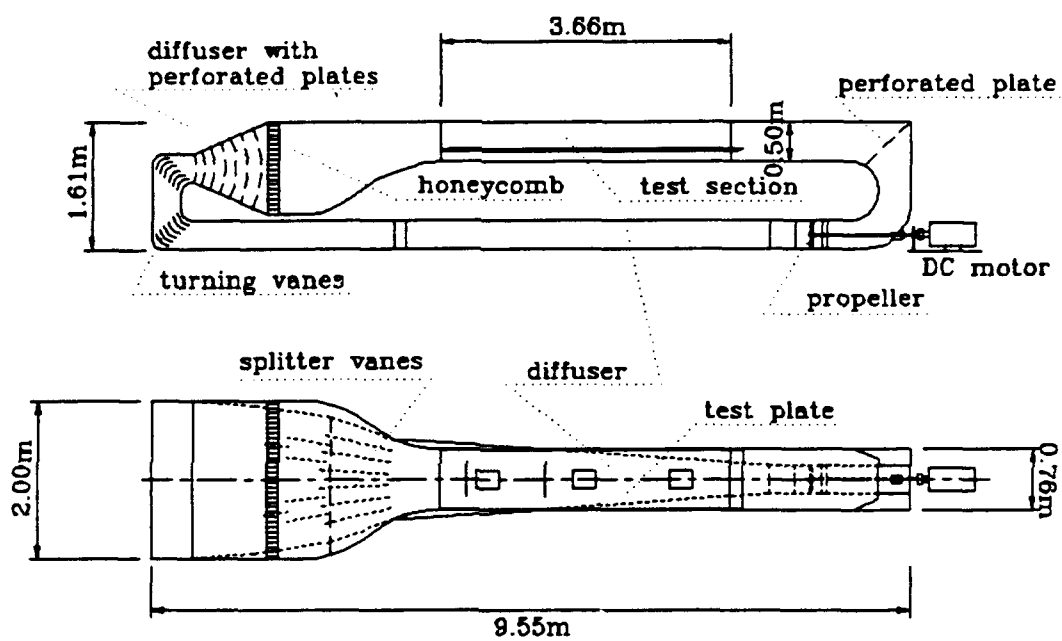
CHAPTER 2

FACILITY

2.1. Laminar Flow Open Surface Water Channel

The automated hydrogen bubble wire technique is being developed for use in the Aerospace Engineering Laminar Flow Water Channel (figure 2). The test section is 3.66 m long and has a nominal cross sectional area of 0.387 m^2 , which varies with water height in the test section. The plate is 1.9-cm thick hard anodized aluminum and runs the length of the test section. The test section has many features to control the conditions of the flow. The plate has an elliptical leading edge and an adjustable tail, 15.2-cm chord, on the trailing edge which is used to position the stagnation point on the upper side of the leading edge to prevent any separation that may begin there. Running the length of the test plate are side bleed slots which can be adjusted to suppress side wall contamination. On the plate itself are two dye slots for visualization, three plexi-glass windows, and several plexi-glass circular ports. The walls of the test section are made of 1/2" thick glass. Access to any part of the test plate is achieved from beneath the plate.

Extending beyond the test section 1.22 m is an open channel which acts as a buffer to isolate the test section from any secondary flows in the first turn. At the first corner is a 0.159 cm (1/16") thick stainless steel perforated plate which aids the turning through the open surface corner. This plate has 0.3175-cm (1/8") perforations and an open area of approximately 64%. The first turn contracts to the



Laminar Flow Water Channel

Figure 2. Aerospace Engineering Laminar Flow Water Channel.

cross sectional area of the pump. The pump is a boat propeller with a 33-cm diameter and is powered by a 7.5-hp DC electric motor.

The lower leg of the flow loop is comprised of a diffuser which extends 4.57 m (180"). It is followed by a second diffuser with three stages of splitter vanes to prevent wall boundary layer separation. From this diffuser the flow turns up through two constant-area corners with the assistance of two sets of turning vanes.

The flow leaving the second set of turning vanes immediately enters a wide-angle diffuser which increases the flow area from 0.356 m^2 to 1.143 m^2 . This expansion decelerates the flow so that the flow conditioning devices downstream do not cause a large head loss. This diffuser is equipped with seven perforated plates with a 64% open area (.159 cm thick [1/16"], .3175cm [1/8"] perforations) which re-energize the wall boundary layers and prevent them from separating. Any wakes produced by the turning vanes are broken up by the perforated plates so that the flow is smooth upon leaving this wide angle diffuser section.

Just after the diffuser plates comes the settling section. In this section lies the flow conditioning which includes a 6-in. honeycomb section with 0.3175-cm (1/8") cells, and the provision for five fine-mesh screens to be installed at a future date. Completing the flow passage is a 6:1 contraction leading to the test section.

2.2. Hydrogen Bubble Apparatus

2.2.1. Design Specifications

Since others have designed and built hydrogen bubble wire systems, it became apparent that there would be no radical design changes in the overall concept. By investigating designs by Schraub et al. (1965), Kim et al. (1971), Matsui et al. (1977), Clutter and Smith (1961), and Lu and Smith (1985), it was determined that a system could be developed which could capitalize on much experience gained from their designs.

Matsui et al. (1977) did a study on the effects of electrode material and electrode size to determine the effects on the production of hydrogen. They experimented with two wires, a 30- μm diameter platinum and a 10- μm tungsten wire. On the 30- μm wire, extremely small, densely spaced bubbles were generated at the surface. Neighboring bubbles combined into larger ones, and in the course of time the number of bubbles decreased. Their sizes were not uniform, being 0.5 to 1.5 times the diameter of the wire. The 10- μm wire was quite different; bubbles generated near the wire were evenly distributed and did not coalesce. Matsui et al. also noted that their size also remained fairly uniform. They concluded that in a low speed flow a sufficiently thin generating wire is superior for generating the smallest bubbles. In addition, these bubbles will be least affected by buoyancy. Matsui et al. (1977) obtained the best results using tungsten wire. Schraub et al. (1965) noted that the material used to make bubble generation wires is not critical except with respect to corrosion and fragility. Stainless steel wires are usually strongest and

easiest to handle. Platinum is usually preferred because it does not corrode, and it appears to accumulate dirt less rapidly (Schraub et al. 1965). Due to experimental considerations, the material chosen for the wire was stainless steel because of its strength. Two wire sizes were tested to optimize performance, 0.002 in. and 0.001 in. The 0.001-in. (25- μm) stainless steel wire was not strong enough to handle the force of the oncoming flow, and would yield regardless of tension. The 0.002-in. (50- μm) wire held its perpendicular position and produced bubbles which were more than adequate for this study.

The local water supply was fairly hard and appeared to produce bubbles easily. It was preferable to avoid introducing substances into the channel in order to enhance bubble formation, because the test plate was made of aluminum and corrosion was a major concern. The closed-loop, open-surface water channel provided fast recirculation of the electrolyte and prompt removal of the gas and vapor bubbles from between the electrodes. The future addition of a de-aerator will further reduce the developing gas in the electrolyte. With the above electrolysis conditions established, the laminar water channel was well suited for the use of the hydrogen bubble technique.

As stated above, the design is applicable over a wide range of operating conditions. Guidelines were set to limit the ranges of operating conditions for various aspects of the electrical circuit. The dc voltage must range from 0 to approximately 100 volts, the pulse width must range from 1 to 9 ms, and the frequency was fixed at 30 Hz. The frequency was dictated by the framing speed of

the video camera. The synchronization of the bubble wire and camera sync pulse will be described below.

2.2.2. Apparatus Design

The final design is similar in function to that of Schraub et al. (1965) and Lu and Smith (1985) but is comprised of components including the logic and analog output of a computer to perform the "electrical circuit equivalent" rather than using an individual circuit to perform the entire experiment independently. As shown in figure 3, there are several components which have been combined to perform the hydrogen bubble measurements. In the closed loop process, the video camera records an event which it triggers. The process begins with the video out signal from the camera. This signal is filtered by a DISA bandpass filter with inversion capability and then further conditioned by a signal conditioning circuit. This signal triggers the DAS-16 through its digital input port. The DAS-16 sends out a 5-volt pulse to the triggering side of a solid state dc relay. The solid state relay then switches a 95-volt DC source on to the bubble wire. The bubbles due to the pulse are then recorded by the video camera and the "cycle" begins again. This "cycle" takes place at the camera's framing rate of 30 Hz.

2.2.2.1 Video Camera Trigger

In order for the data acquisition procedure to work to its potential, the events from the actual video taping to the bubble production must be in synchronous

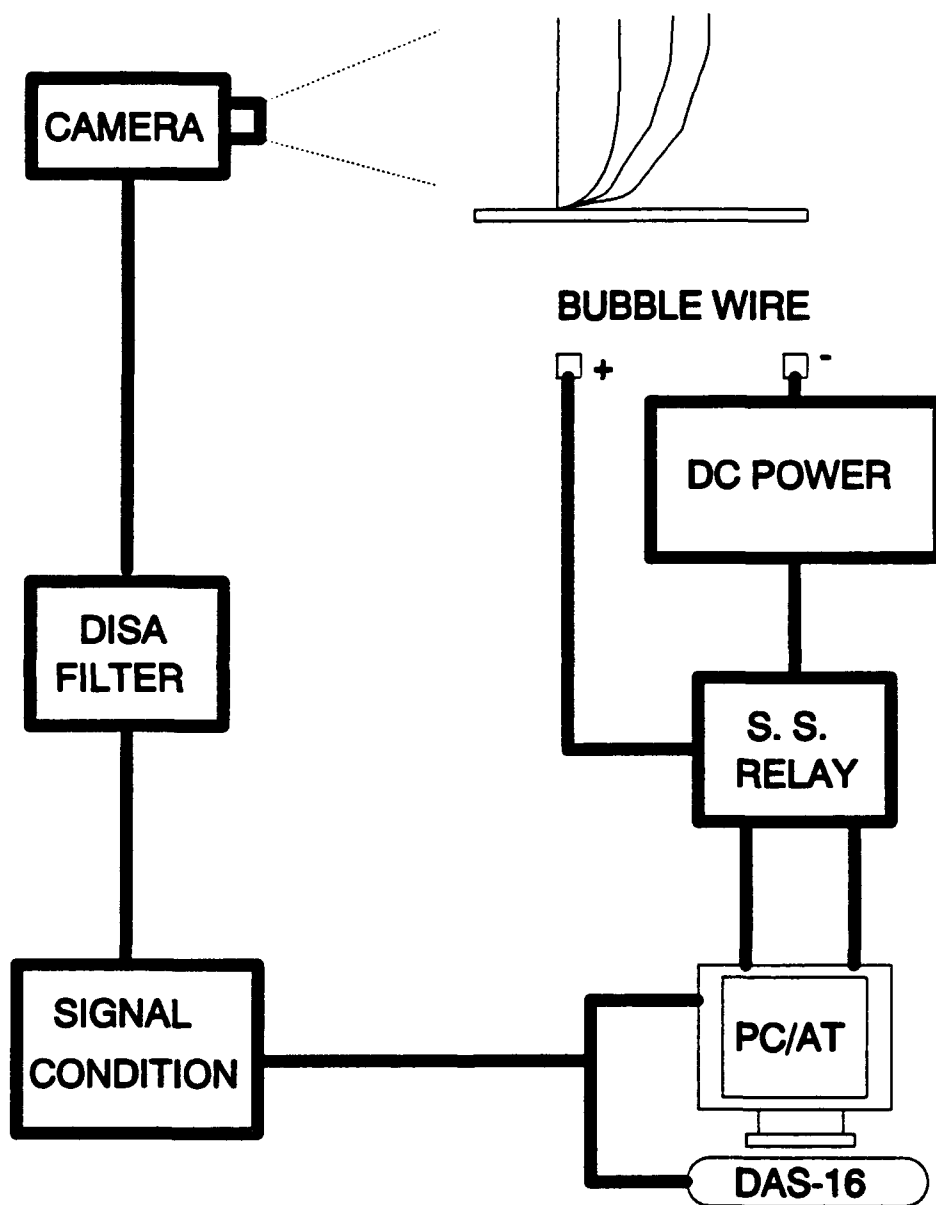


Figure 3. Hydrogen Bubble System Flow Chart.

operation. At each new video frame the bubble line must be at the same "growth" stage. In order to achieve this coordination the camera must trigger the bubble production.

The video camera is a SONY video 8 Handycam/pro which puts out an National Television Standards Committee, NTSC, composite video signal, which meets Electronic Industries Associated, EIA, standards. The video signal from the camera is used to trigger a MetraByte DAS-16, which is a multifunction high speed analog/digital, input/output, expansion board. The DAS-16 board is installed in an IBM PC AT and is the control unit which pulses the hydrogen bubble wire.

2.2.2.2 Signal Conditioning

To understand how the camera video signal triggers the DAS-16, one must understand the television or video system. A video "picture," or frame, is made up of 525 lines of information separated into two fields. These two fields are interlaced together to form the frame. The first field has horizontal lines at the odd lines (e.g., 1,3,5...), and the second field has horizontal lines at the even lines (e.g., 2,4,6....). Synchronization of the two fields allows for the alignment of the interlaced lines and produces an undistorted picture.

An electron beam gun inside the monitor scans across the picture tube exciting the phosphorous elements in a tube. The scanning beam must reassemble the picture elements on each horizontal line with the same left-right position as in the original image at the camera tube. The same must hold true for the vertical

position of the picture. A horizontal synchronizing pulse is transmitted in the video signal for each horizontal line, in order to keep the horizontal scanning synchronized. Similarly, a vertical synchronizing pulse is transmitted in the video signal for each field, to synchronize the vertical scanning (Grob, 1984).

The video signal is made up of the video information, the vertical sync pulses, and the horizontal sync pulses (figure 4). The horizontal and vertical sync pulses act so that when the electron beam gun encounters one of the sync pulses, it knows whether to end a line and go to the next, or finish a field and start the next.

The framing rate for television sets is 30 Hz. This frequency allows the picture to be jitter free. Within the 30-Hz cycle, the electron beam gun must go from left to right, and from top to bottom on the tube for each field. The two fields are interlaced to create a single picture on the tube within 1/30 of a second.

In order for the electron beam gun to respond to the sync information, this information must come at a separate frequency. Since the framing rate is 30 Hz and there are two fields per frame, the field rate is 60 Hz. This 60-Hz frequency is better known as the vertical scanning synchronization, or vertical sync. There are 525 complete horizontal lines in each frame. In one second the number of complete horizontal lines scanned must equal 15,750, yielding a horizontal synchronization frequency of 15,750 Hz.

To use the camera to trigger the hydrogen bubble wire through the DAS-16, the video signal from the camera needed to be conditioned. Since the framing rate of the camera is 30 Hz, the production of bubble-lines should also be at 30 Hz. The

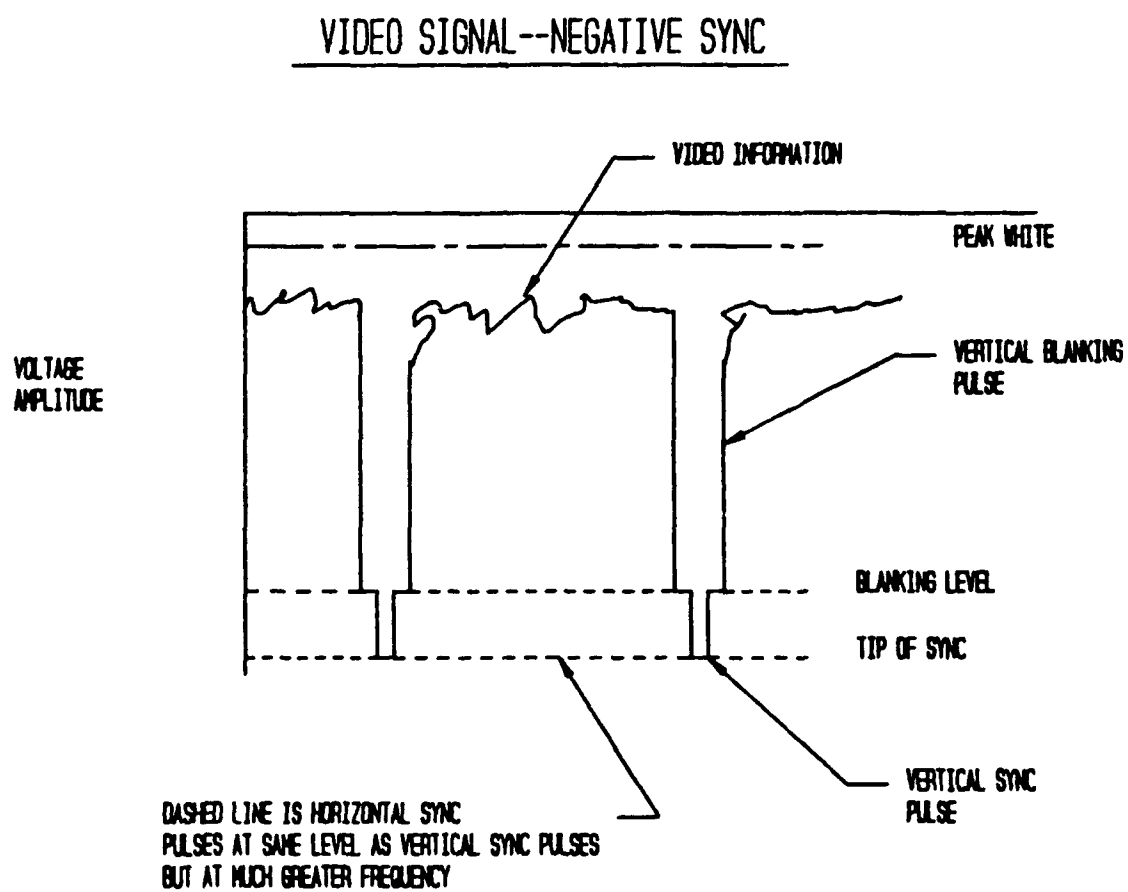


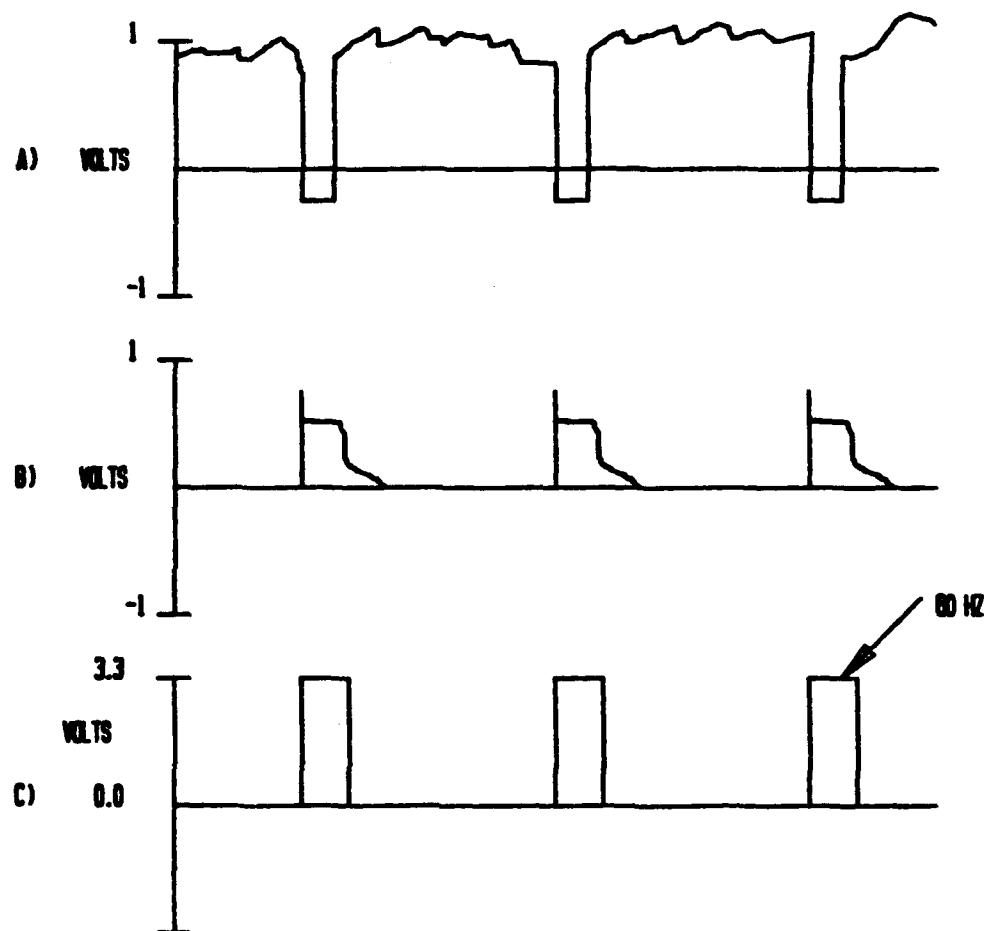
Figure 4. Composite Video Signal-Negative Sync.

vertical sync pulse is a 60-Hz pulse and it is used for this purpose. To accentuate the vertical sync pulse the video signal was filtered using a DISA bandpass filter and inverted. This yields a positive pulse signal (figure 5b). Filter settings are 0.5-kHz low pass and 20-kHz high pass, with the maximum gain possible. The signal is clipped using a diode at 0.7 volts. Because the DAS-16 needs a 2.0-volt signal to trigger its digital input port, an NTE 941M frequency compensated op amp with a gain of 11 is used to amplify the signal. Finally, a zener diode clips the signal at 3.3 volts to yield a clean trigger signal (figure 5c). The circuit is shown in figure 6.

2.2.2.3 DAS-16 and DC Power

The DAS-16 is controlled using the Quinn-Curtis subroutine library called from Turbo-Pascal computer programs. Software was written to control every aspect of the experiment. The pulsing frequency and pulse width were user controlled and delay loops were available if needed. The main logical sequence followed by the software is as follows: The digital input port is scanned until it receives a "high" voltage greater than 2.0 volts. When this trigger is received, a specified voltage is sent to the analog output for a user defined period of time. To utilize the 60-Hz vertical sync to produce a 30-Hz trigger signal, every other pulse must be used. Therefore, the pulsing loop in the software has an additional delay which allows every other vertical sync pulse to pass before again scanning the digital input. The 0-5 volt pulse produced by the DAS-16 analog output is sent to an NTE Solid State DC relay. The relay then switches on a 95-volt DC source to drive the wire.

VIDEO SIGNAL CONDITIONING



A) VIDEO SIGNAL OUT OF CAMERA

B) SIGNAL FILTERED AND INVERTED

C) SIGNAL CONDITIONER WITH AMPLIFICATION
AND ZENER DIODE CLIPPING AT 3.3 VOLTS

Figure 5. Video Signal Conditioning.

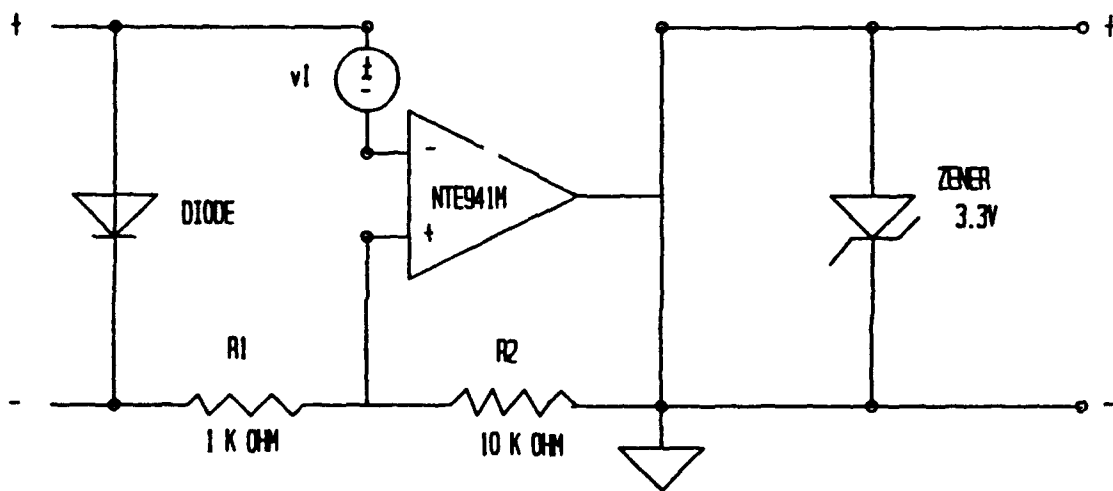


Figure 6. Signal Conditioning Circuit Diagram.

2.2.2.4 Experimental Setup

The hydrogen bubble wire is attached inside a thirteen-thousandths inch hole in a surface mounted port in the test plate and held in place by a set screw with an electrically insulated rubber end. The hole in the port is sealed to eliminate leakage caused by any pressure differential across the hole. The sealed hole prevents a jet of bubbles from escaping through the hole and interrupting the bubble time lines.

The wire is held above the test section by a specially designed holder which has three degrees of freedom and a feature to adjust and maintain the wire tension (figure 7). The tension feature is important since, the wires decay with use and lose their tension.

Lighting was provided from the opposite side of the test section using a 150-watt arc lamp which focused the light into a circular beam. A convex lens was positioned in front of the lamp to further focus the light to the point of interest. Many orientations of the light source were tried. It was found that positioning the light at approximately 45 degrees off-axis in a forward scatter orientation, pointing downstream, provided the best lighting for the procedure. A 150 watt spotlight was oriented 45° off-axis pointing upstream, to saturate the wall region with light, figure 8.

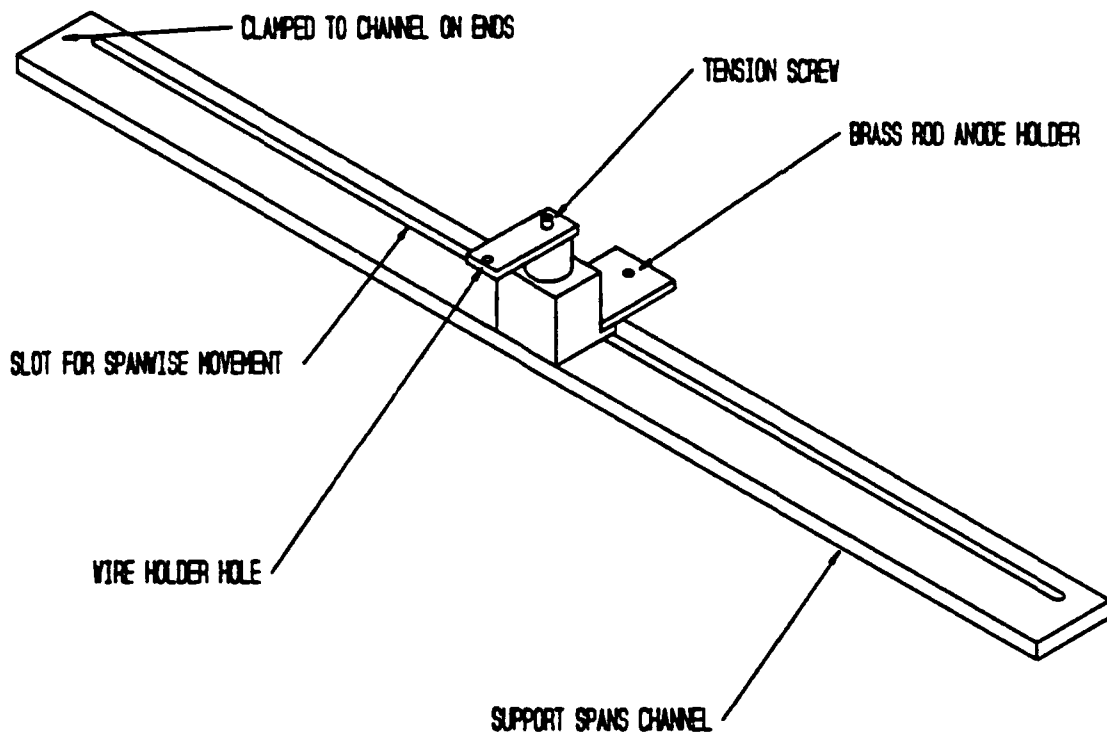


Figure 7. Bubble Wire Holder.

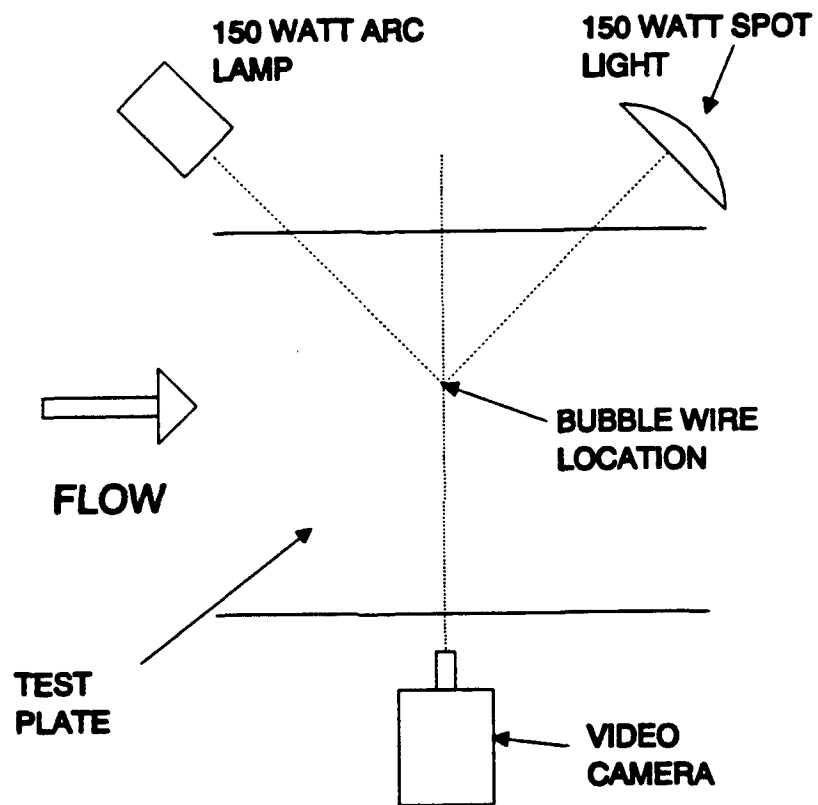


Figure 8. Experimental Lighting Configuration.

2.3. Digital Image Processing

2.3.1. Processing System Overview

An image processing system made by Data Translation in Marlboro, MA was used to convert hydrogen bubble pictures to digital images. The processing hardware included a DT2871 (HSI) Color Frame Grabber, a DT2869 Video Decoder/Encoder, and a DT2858 Auxiliary Frame Processor board. All were operated by a Dell Corp. 310 computer with a Super VGA color monitor and a Mitsubishi Diamond Scan video display. The image processing hardware is controlled using a software package called Aurora tm, also from Data Translation.

Color video signals are transmitted as unique combinations of red, green, and blue (RGB) light. Individual red, green, and blue signals are digitized separately and then converted to hue-saturation-intensity (HSI) data before storage in the three separate frame buffers needed to describe the color image. The HSI color representation of the image closely approximates the way humans perceive and interpret color (Aurora Manual 1989, p. 7).

Hue is a color attribute describing a pure color such as a pure red, or pure yellow, etc. Saturation is also a color attribute. It describes the degree to which a pure color appears to be diluted with white. A highly saturated color appears to have little white content, while faded colors are considered less saturated. Intensity is a color-neutral attribute describing relative brightness or darkness. The intensity of a color image corresponds to the gray-level (black and white) version of the image.

The Aurora package is a comprehensive software subroutine library for digital

image processing with the DT2871, DT2869, and DT2858. Using this software it is possible to capture and display color images in real time in either the HSI or RGB color domain. The routines perform processing and analysis operations such as arithmetic, logical, statistical, or filtering operations on HSI or RGB color images.

The DT2871 (HSI) Color Frame Grabber board captures and displays images in real time. It converts RGB to HSI and vice-versa. On this board the image data is stored in three separate 512 x 512 x 8 bit buffers, one for hue, one for intensity, and one for saturation. The color image is viewed by simultaneously displaying the contents of these three buffers. The DT2871 also has a fourth 512 x 512 x 8 bit buffer containing four 1-bit overlay bit planes which can be used for temporary storage of intermediate calculations during processing operations.

The video input signal from the Sony Handycam/pro is an NTSC composite type which is compatible with the DT2871. The DT2869 converts NTSC composite color video input into the RS-170 RGB format. The DT2869 is also used to convert the color image output from the DT2871 into an NTSC format when using a video display device requiring an NTSC format.

The DT2858 Auxiliary Frame Processor is a board that works in conjunction with the DT2871. The DT2858 can perform mathematically-intensive operations on individual frame buffers at high speeds, greatly accelerating execution time. Each Aurora image residing in the on-board memory buffers of the DT2871 or in extended memory requires 1 Mbyte of contiguous memory. Each individual frame buffer requires 256 Kbytes.

2.3.2. Still Image/Time Base Correction

Vertical and horizontal synchronization information is critical in forming a high quality image. When the sync signals are not of the proper form or are missing, the image can exhibit many problems such as skewness, jitter, or missing information. For the hydrogen bubble technique of flow measurement to work, each frame must be viewed and analyzed individually. The Sony camera has a freeze frame and frame advance capability and serves as the video playback machine with the needed features. Unfortunately, when the camera is in the pause or freeze frame mode the DT2869 cannot convert the NTSC composite video with all its sync information into the RS-170 format. The DT2871 therefore receives an image with many or all of the picture problems listed above.

To correct for the incompatibility between the camera and the frame grabber when the camera is in pause mode, an IDEN IVT-7 Time Base Corrector (TBC) was installed between the two. The TBC strips the incoming sync information from the video signal and replaces it with an RS-170 RGB sync signal. This allows the signal to match the DT2871 requirements. The TBC also has a frame/field freeze to enhance the image by removing jitter and/or skewness. Even after correction, the DT2871 sometimes has trouble completely aligning the two fields of a frame since it has two frozen fields that it is continually trying to align. To prevent this small amount of jitter, the TBC field freeze capability is used which allows the DT2871 to freeze one field and align the other field to the frozen field. With the TBC correcting all incompatibility between the video input signal and the frame grabber, a

quality image is captured and prepared for manipulation to obtain the desired flow description.

2.3.3. Image Processing Procedure

For the procedure to calculate velocity, the location of the edges of each timeline must be established and the corresponding distance between the timelines calculated. There are several techniques to detect edges in an image. Vertical line enhancement, optimal thresholding of edge regions, and gradient/Laplacian techniques were all investigated.

Vertical line enhancement is designed to highlight lines that are one pixel wide. This technique is not effective for the hydrogen bubble technique because the width of the bubble timelines is generally several pixels wide. Optimal thresholding is a technique which statistically analyzes a histogram of the intensity values in a region of interest. The problem with this technique was that non-uniformity in lighting, from the wall into the freestream, spanned the entire intensity spectrum. This non-uniformity lead to situations where noise in the freestream had a higher intensity value than the timelines in the wall region. If a threshold was set for the wall region, the software would recognize noise as a timeline in the freestream, and this would generate substantial error. The gradient/Laplacian method yielded the least error since it utilizes the intensity distribution across a row of pixels corresponding to a single distance from the wall in order to find the edges.

The gradient/Laplacian process yields the edge locations of bubble lines by

locating the points along the maximum negative intensity gradient. This technique is similar to the technique developed by Lu and Smith (1985). The maximum negative intensity gradient is the leading edge of the bright timeline on the dark background. The intensity distribution across a row of pixels in an image has a sinusoidal shape (figure 9a). The high intensity represents a bright bubble-line and the low intensity represents a dark background. Taking the first derivative of this distribution yields the gradient, or slope of the line. Taking the derivative of the gradient, or the second derivative of Intensity, yields the position where the maximum of the first derivative is located. This position would be the edge of a timeline.

To calculate the velocity throughout the boundary layer, the first three bubble lines in each image were analyzed. The first bubble line in every frame is a cloud of bubbles still attached to the wire. The second timeline is free of the wire but has not moved through a complete time interval at the time of the exposure. The period between the wire and the first timeline is unknown because of the lag between the camera triggering the DAS-16 and the next shutter opening. In addition, it is difficult to predict the period needed for the bubbles to form on the wire. The period between the second and third timelines is a complete 33.33 ms, the framing rate of the camera.

The image of interest was frame-advanced to the frame grabber using the camera frame advance capability. This image was captured by the frame grabber and separated into the intensity, hue, and saturation buffers. The hue and saturation buffers were cleared leaving only the black and white version of the image. The hue

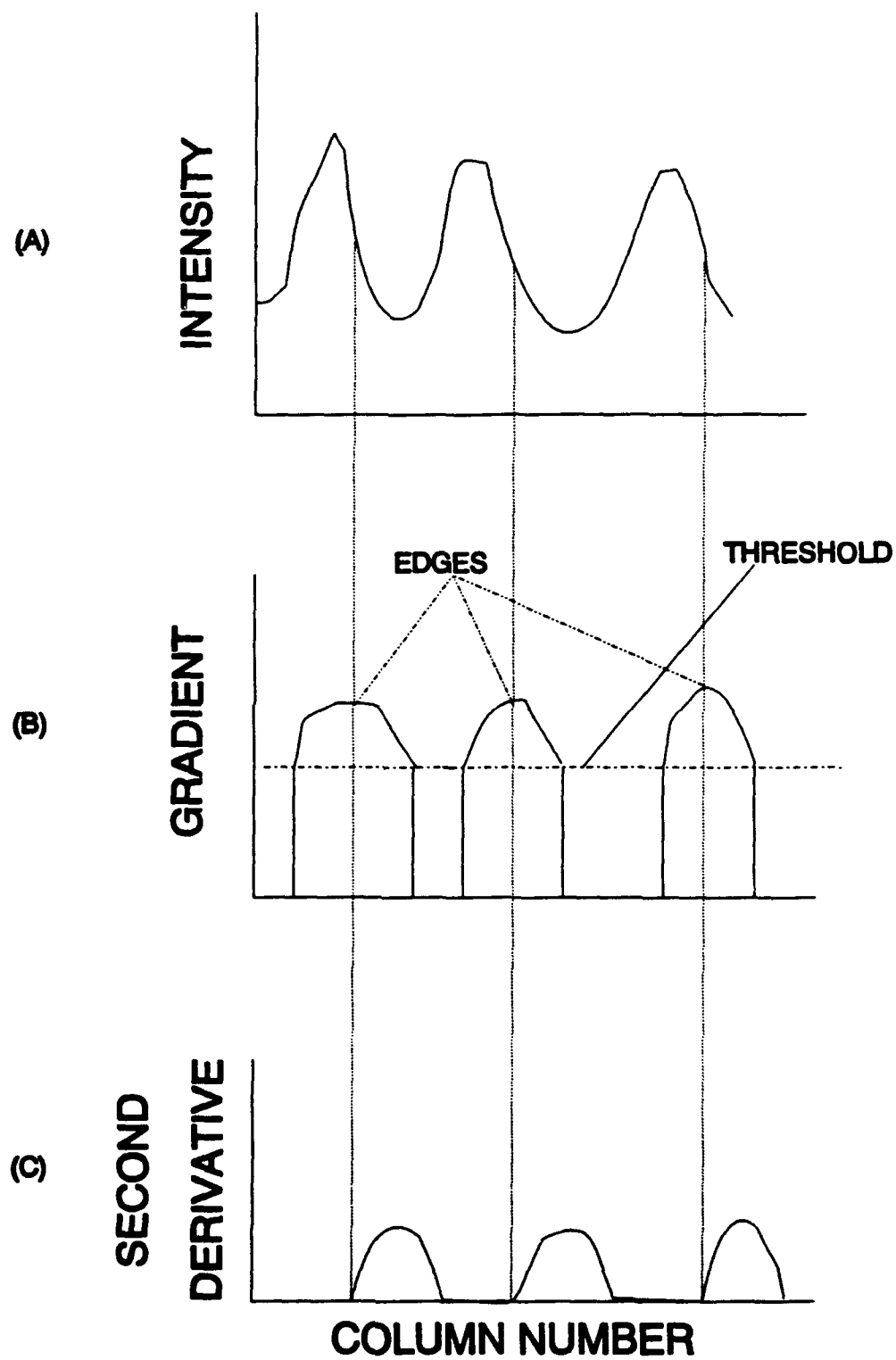


Figure 9. Edge Detection Scheme.

and saturation buffers as well as the auxiliary buffer were then used as intermediate calculation buffers in the procedure.

Each row of the intensity buffer was lowpass filtered using the coefficient mask in figure 10d. The gradient, or derivative, across this row was then taken using the mask in figure 10e. Since noise components also yield gradients, the software might recognize these noise components as timeline edges. To overcome this problem, the fact that the gradient at a timeline edge is much larger than the gradient of a noise component must be utilized. The mean of the gradient values across a row was calculated. Each pixel within that row was then tested against this mean value. If the value was above the mean, it remained unchanged. If the value was below the mean, it would then be set to zero. This procedure is known as threshold filtering. Figure 9b demonstrates the procedure. All the gradients due to noise would typically fall beneath the mean value threshold. With this "cleaned" gradient distribution, another derivative would be taken to yield the maximum values. This derivative coefficient mask is shown in figure 10f.

Once the edge points have been found by the software, the intensity buffer is set to zero, and these edge pixels are assigned a value of 255, or white. Since there are discontinuities in this trace of the edges due to lighting irregularities, another lowpass filtering is performed using the mask in figure 10c, leaving a continuous profile. Measuring the distance between the second and third lines is done by counting the pixels between the two and applying the correct pixel scaling to obtain the true distance.

A	B	C
D	E	F
G	H	I

(a)

W1	W2	W3
W4	W5	W6
W7	W8	W9

(b)

1	1	1
1	1	1
1	1	1

DIVISOR
9

(c)

1	1	1
---	---	---

DIVISOR
3

(d)

1	0	-1
2	0	-2
1	0	-1

(e)

0	0	0
1	0	-1
0	0	0

(f)

Figure 10. Coefficient Masks for Image Processing.

To understand the calculation procedure, specific details of the coefficient masks must be specified. Coefficient masks, or convolution masks, are digital coefficient arrays which are applied to a given pixel and its neighbors (figure 10a) to obtain a weighted quantity. Each element in the pixel neighborhood, A - I, is multiplied by its respective weighting coefficient, $W_1 - W_9$ (figure 10b). The result of this multiplication replaces the value at the center of the mask, I_{ij} , i.e.:

$$I_{ij} = W_1A + W_2B + W_3C + W_4D + W_5E + W_6F + W_7G + W_8H + W_9I \quad (3)$$

Low pass filter masks operate simply by multiplying each neighbor by 1, adding them and dividing by the number of neighbors. This is known as neighborhood averaging. The gradient masks used here were of the Sobel operator type. The first gradient was obtained using a full 3 x 3 Sobel operator shown in figure 10e. It smoothes noise and provides the gradient in the x direction. The Sobel operator is essentially a central difference method:

$$\frac{\partial I}{\partial X} = \frac{I_{I+1,J} - I_{I-1,J}}{2\Delta X} \quad (4)$$

The weighting of the Sobel operator increases the smoothing of the neighboring pixels making the derivative less sensitive to noise. Weighting the pixels closest to the center yields additional smoothing (Gonzalez and Wintz, 1987). The second

gradient mask, figure 10f, is a simplified Sobel operator and is the central difference method.

Lowpass filters, or averages, were chosen over median filters because they would smooth the intensity distribution leaving the overall shape of the distribution unchanged. Median filters have the possibility of altering the overall shape of the distribution especially at the edge locations.

As mentioned above, the velocity is measured using time of flight techniques. This measured velocity, U_b , is then corrected for wake effects using the velocity correction procedure described in section 1.5. Since the lighting non-uniformity is dominant in the region very close to the wall, 0 - 4 mm, the processing software has difficulty interpreting the bubble timelines. Schraub et al. (1965) noted that the bubble buoyancy effects could be neglected when the ratio of the vertical terminal velocity to the local velocity is below 1/50. This velocity criteria was used to establish the limits of a third order polynomial least-squares curve fit to extend the profile down to the wall. The velocity criteria was reached approximately at the location where the lighting became too faint for the software to detect the timelines. The above procedure yielded the instantaneous u , or streamwise, component of velocity, $u(y,t)$. At the completion of this calculation for each frame, instantaneous displacement thickness, δ^* , and momentum thickness, θ , were calculated for the profile using:

These quantities are important in relating the boundary layer characteristics to the bulk effects that the boundary layer has on the outer flow which are responsible for

$$\begin{aligned}\delta^* &= \int (1 - \frac{u}{U}) dy \\ \theta &= \int \frac{u}{U} (1 - \frac{u}{U}) dy\end{aligned}\tag{5}$$

momentum transfer and far-field noise generation.

CHAPTER 3

RESULTS AND DISCUSSION

To evaluate the accuracy of the image processed hydrogen bubble technique as a measurement tool, a thorough investigation was undertaken of each aspect of the procedure. The first test was to analyze an analytical Falkner-Skan profile. Digital image processing of a paper-plotted profile showed the accuracy of the method, without the errors due to irregularity in bubble formation or uncertainty due to wire interference. This established how well the image processing technique could recognize an edge of known sharpness. It also established the magnitude of the error due to limitations in the resolution from finite pixel spacing. The next step was to analyze all of the errors due to the unique flow regime. This analysis was similar to Schraub et. al. (1965) and resulted in an estimate of the error due to the trajectories of the hydrogen bubbles and the bubble wire. After all of the uncertainties were accounted for, the method was tested against a laser Doppler anemometer (LDA) for both steady laminar and unsteady turbulent spot flows.

For the steady laminar case the LDA data was obtained by time averaging over thirty (30) seconds. Instantaneous Hydrogen bubble wire profiles as well as one and two second time averages (30 and 60 profiles) were compared to this LDA data for a range of velocities. For the unsteady turbulent spot flows, ensemble averaged and instantaneous δ^* vs. time realizations were compared to ensemble-averaged δ^* vs. time obtained using the LDA. Ensemble averaged velocity profiles for each

technique were compared at several instances throughout the spot passing.

3.1. Falkner Skan Velocity Profile Test

The accuracy of the image processing system is the largest factor limiting the potential precision of the technique. To obtain a benchmark accuracy of the image processing procedure, a known profile was plotted, videotaped and processed. Analyzing this profile isolates the image processing procedure from the bubble generation processes and has negligible data variability. The analytical description of the flow used to generate the test profile is also available for evaluating the image processed data.

A Falkner Skan similarity flow was used as the known profile. Falkner Skan parameters $\beta = 1$ and $m = 2$, representing flow against a wedge of half angle of $\beta\pi/2$, were chosen arbitrarily to generate the shape of the profile used for analysis. This plot was then videotaped and image processed to obtain results for comparison with the known solution. The results of the comparison are relatively good with an overall average error of 1.4728% (figure 11). At distances from the wall greater than 0.1 cm, the percent error is generally within $\pm 1\%$. This is especially good in the strong gradient section of the profile. Below 0.1 cm the process loses accuracy due to the technique itself. In this region several time lines mesh together forcing the horizontal scanning technique to have trouble resolving a distinctive pattern. As mentioned above, Lu and Smith (1985) also had a problem resolving timelines in the inner region of their turbulent boundary layer. The results obtained by this test

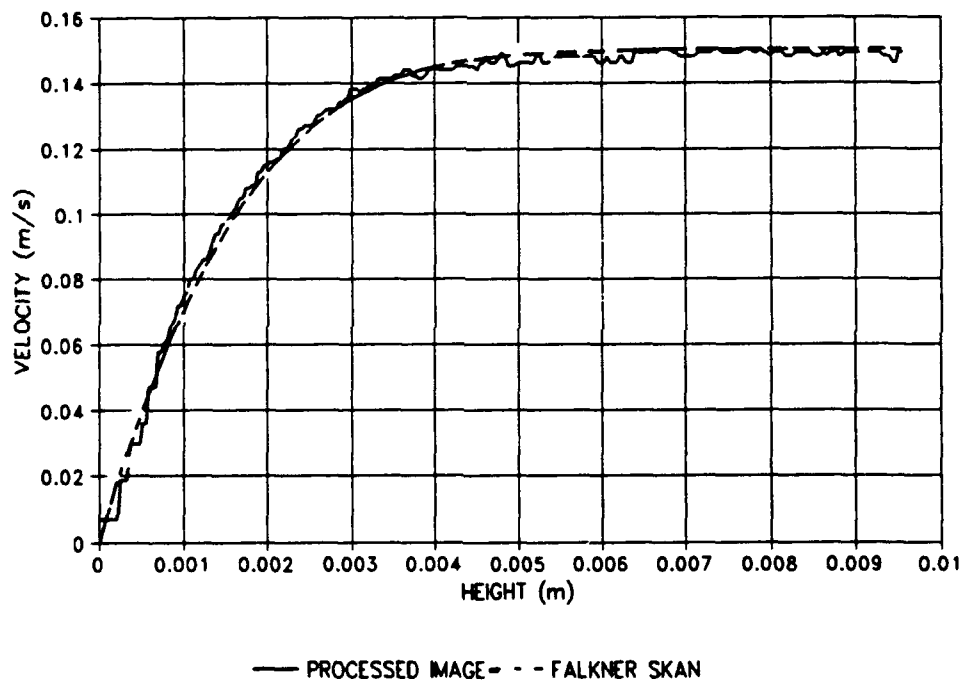


Figure 11. Falkner Skan Actual and Processed.

represent the best possible accuracy of the procedure using our hardware. The resolution within the gap between two bubble lines in the sample image was approximately 110 pixels at the top of the boundary layer and zero pixels near the wall. This is an important parameter since the possibility of being one pixel off from the true edge of any timeline carries a much larger error in the velocity calculation if that one pixel is one pixel in 20 pixels rather than one pixel in 110 pixels. In the actual images, it was required that the camera field of view be approximately 4 cm above the plate to ensure that the entire spot disturbance be seen. Because of this requirement, the timeline separation was limited. If the scope of this study was only laminar profiles, the region of interest would have been about 2 cm high, and then a greater resolution would be possible. Pixel resolution between timelines in the actual images ranged from 32 pixels at 15 cm/s to 48 pixels at 22.2 cm/s in the freestream. This resolution leaves an error band of approximately 2%-3%.

3.2. Analytical Uncertainty Analysis

In order to evaluate the full potential of the hydrogen bubble wire method, an estimate must be made of the error by tracking bubbles. The hydrogen bubble wire technique has many possible error sources associated with it. Schraub et al. (1965) listed several contributors to this error. The present study encountered many of the same errors and several new errors due to the advancement toward automated digital image processing.

As detailed above, the velocity at the wire location is obtained by the

reduction of data from the timelines using equation 6.

$$U_b = \frac{\Delta X}{\Delta t} \quad (6)$$

To obtain the overall error in an instantaneous measurement, the error associated with each component of equation 6 must be identified and taken into account. Following the analysis by Schraub et al. (1965) and Kline and McClintock (1953), the procedure for estimating uncertainties in a result, R, where $R = R(V_1, V_2, V_3, \dots)$ is expressed as,

$$W_R = \left[\left(\frac{\partial R}{\partial V_1} W_1 \right)^2 + \left(\frac{\partial R}{\partial V_2} W_2 \right)^2 + \dots + \left(\frac{\partial R}{\partial V_n} W_n \right)^2 \right]^{1/2} \quad (7)$$

where W_1, W_2, \dots, W_n are the uncertainty intervals in the corresponding variables V_1, V_2, V_n . Uncertainty intervals are the estimated confidence intervals about the expected value of each variable given at some odds. Schraub et al. (1965) gave 20:1 odds. To estimate the uncertainty in U_b , the partial derivatives in equation 7 can be evaluated from equation 6 where $U_b = U_b(\Delta X, \Delta t)$, i.e;

$$\frac{W_u}{u} = \left[\left(\frac{W_{\Delta X}}{\Delta X} \right)^2 + \left(\frac{W_{\Delta t}}{\Delta t} \right)^2 \right]^{1/2} \quad (8)$$

Since the uncertainties in each of the variables are combined by the sum of their squares, any terms which are less than one-fifth of any other term can be considered negligible without any loss of significance (Schraub et al., 1965). Schraub et al. (1965) found that errors associated with Δt and the scaling factors associated with ΔX were negligible compared with the errors in ΔX itself. The same observations apply

here. Therefore, the major contributor to the overall error is in the ΔX term.

The total uncertainty in the ΔX term is comprised of several separate uncertainties arising from:

1. Measurement of ΔX in the digitized image
2. Averaging effects in a changing velocity field
3. Response time of bubbles to fluctuations
4. Bubble rise velocity
5. The uncertainty in calculating δ^* and Θ from the velocity
6. Velocity defect behind the wire

The error in measuring ΔX due to limitations in the available number of pixels between timelines was outlined in the Falkner Skan section, section 3.1. As described above, the error associated with this measurement is between 2% and 3%.

The errors of averaging effects arise because the method is predicting the Eulerian velocity field at a point in time and space, $U_b = U_b(x,y,t)$, using the Lagrangian time-averaged velocity of marker bubbles over a small time interval (Schraub et al., 1965). Lu and Smith (1985), however, assumed that the Eulerian field velocity equaled the Lagrangian time-averaged velocity due to the short distance and averaging time. They concluded that their results substantiated this assumption. The results of the present study outlined below also substantiate this assumption.

The error due to limitations in response of the bubbles to fluctuations was shown by Davis and Fox (1967) to be negligible as the bubbles could reach 98% of the fluid velocity in 0.1 ms. The response of the bubbles to buoyancy could not be

neglected however.

As mentioned in section 2.3.3, Schraub et al. (1965) suggested the use of a correction when the vertical rise velocity divided by the mean velocity was above 1/50. They also determined that the bubble diameter ranged from 1/2 to 1 wire diameters. Based on one wire diameter of 50 μm , the terminal rise velocity was calculated at 0.0014 m/s. Therefore, when the mean velocity, $u(y,t)$, fell below 6.8 cm/s, a third order polynomial least-squares fit was employed to fit the profile down to the wall. The third order curve fit had the form,

$$U = C_1 y^3 + C_2 y^2 + C_3 y \quad (9)$$

Solving for the constants required using twelve points as sample points for the fit. The first point was $y = 0$, the second was the point at which the 1/50th criteria was met, and the remaining ten points were the ten points above the 1/50th criteria point. Stretching the points up into the profile enabled the portion of the curve fit to better represent the shape of the profile. The laminar profiles detailed below show that the curve fit method adequately corrected the buoyancy effect near the wall.

To obtain an estimate of the error associated with the trajectory of a bubble due to buoyancy, averaging effects, and response, an analytical study was performed. The study included tracking the trajectory of several bubbles in a known flowfield. The motivation was to create a model which would work in the same way as the experimental procedure. The model tracks a bubble for a given period of time in a known flowfield. Following several bubbles yields timelines as in the real

experiment.

The analytical model of the trajectory of a bubble in an unsteady flow was developed and tested. Twenty bubbles were tracked for a time interval of 1/15 seconds. The experimental time interval was 1/30 seconds, however, the second timeline was used for the velocity calculation. This second timeline was approximately 1/15 seconds away from the wire. The velocity at the final y locations of the twenty bubbles was found using equation 1. The velocity profile obtained through the trajectory analysis was then compared to the exact profile from the given flowfield at the given x,y locations at the trajectory completion time.

The analytical model of a bubble in an unsteady flow follows from the studies of Maxey and Riley (1983) and Hoffman (1988). The vector equation for the trajectory of a rigid, spherical bubble in an unsteady flow is as follows:

$$\rho_b V_b \frac{dU_b}{dt} = V_b (\rho_b - \rho_f) g + \rho_f V_b \frac{DU}{Dt} + 6\pi \rho_f \nu_f a (U - U_b) + \frac{1}{2} \rho_f V_b \left(\frac{DU}{Dt} - \frac{dU_b}{dt} \right) \quad (10)$$

(1) (2) (3) (4) (5)

where V_b is the bubble volume, U_b is the bubble velocity, ρ_b and ρ_f are the bubble and fluid density respectively, ν_f is the fluid viscosity, a is the bubble radius, and U is the given flowfield, $U(x,y,t)$:

where ω is determined by the period of the spot passing. The significance of each numbered term in equation 10 is as follows:

$$U = C_1 y^n x^{1/2} \frac{U_\infty}{\text{Dia}^m} (1 + C_2 \cos(\omega t)) e_x - \frac{C_1}{6} y^{n+1} x^{-1/2} \frac{U_\infty}{\text{Dia}^m} (1 + C_2 \cos(\omega t)) e_y \quad (11)$$

1. Mass of the particle times its acceleration
2. Buoyancy term
3. Force due to the pressure gradient in the fluid surrounding the bubble, caused by the acceleration of the fluid.
4. Viscous resistance of the spherical bubble.
5. Force required to accelerate the "added mass"

To complete the system of equations the following is needed:

$$\frac{dx_{bi}}{dt} = U_{bi} \quad (12)$$

where x_{bi} is the position vector of the bubble. The assumptions are that the bubble is rigid and retains its shape. The bubble is also assumed to be a solid sphere which allows the use of the Stokes drag term. Since this part of the analysis is an estimate only, the above method is suitable to establish a best case accuracy estimate for the velocity calculation and the calculation of δ^* from the velocity profile.

Equation 10 was solved using an iterative scheme employing sixty time steps through the 1/15 second travel time. The twenty bubbles were given initial positions from zero for the first bubble to 7.6 cm for the twentieth bubble. The bubbles were spaced 2 mm apart between these points. Each bubble was tracked through the

specified time interval. At the final time step, the final x location was used to calculate the ΔX value and the velocity of the bubble was obtained using equation 1. The twenty bubbles therefore yielded twenty values of $u_b(y,t)$ which could be compared to the actual values of $u(x,y,t)$ from the given flowfield. As mentioned above, this procedure was the exact methodology of the experimental digital image processing technique.

The flowfield was chosen to closely approximate a vortex passing the wire. A flowfield of this type is not exactly the same as the flowfield found during the passing of a spot. However, the flowfield chosen does have vortex characteristics, the strength of which is based on the various constants. To fully investigate analytically the trajectory of the bubbles, several cases were run with various constants changed.

The constants given in the flowfield were adjusted for several reasons. C_1 was calculated for all cases such that the highest initial y position would see a velocity similar to the actual experimental velocity, $U = .1904$ m/s. C_2 determines the magnitude of the time dependent term, and n and m give the y dependence and the proper units respectively. Case 1 used $C_1 = 2.0861 \times 10^{-4}$, $C_2 = 0.02$, $n = 1/2$, $m = 1$, and the time period was from 0 - 1/15 seconds. The velocity error ranged from 0.4% in the freestream to -0.5% near the wall (figure 12). The error in δ^* was 0.3665% of the known solution. Case 2 used $C_1 = 2.0862 \times 10^{-4}$, $C_2 = .02$, $n = 1/2$, $m = 1$, and the time period was from 1.967 to 2.033. This time change caused the cosine

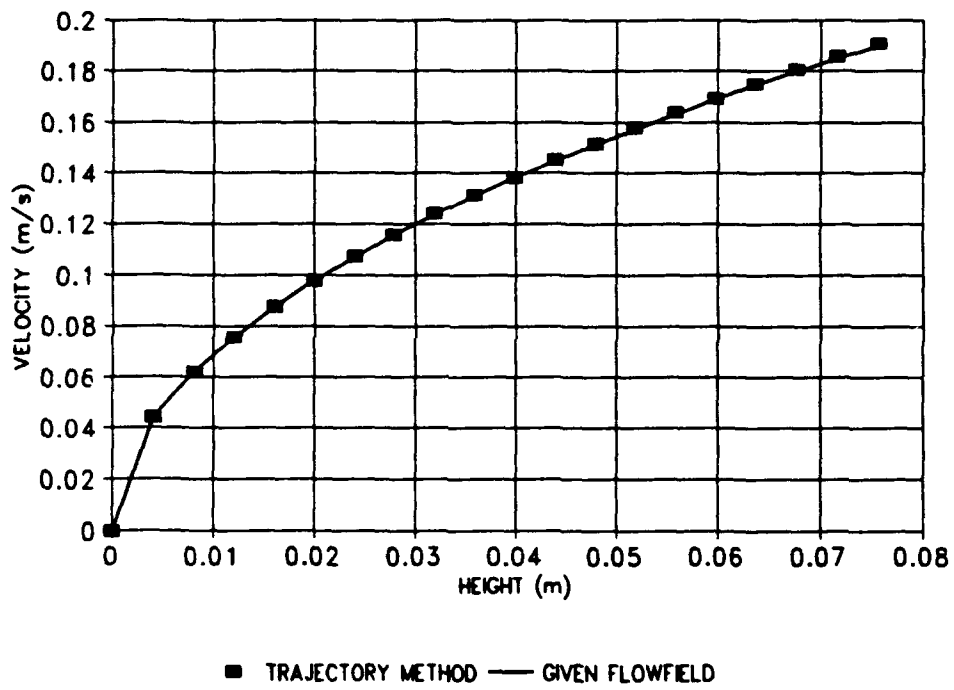


Figure 12. Bubble Trajectory Analysis Case 1.

term to change sign at the mid-time interval. The velocity error ranged from 1.3% in the freestream to 0.3% near the wall (figure 13). Case 3 used $C_1 = 2.0861 \times 10^{-4}$, $C_2 = .2$, $n = 1/2$, $m = 1$, and the time period was from 1.967 to 2.033 seconds. The velocity error for case 3 varied from 0.9% in the freestream to 0.02% near the wall (figure 14). The error in δ^* was 0.3573% for case 3. Cases 1 through 3 did not vary the flowfield that drastically. Therefore, to substantially change the flowfield, the constants were $C_1 = 2.36 \times 10^{-9}$, $C_2 = .02$, $n = 2$, $m = 2.5$, and the time period was from 0 to 1/15 seconds. The velocity error for case 4 varied from 3.5% in the freestream to 1.7% near the wall (figure 15). This case would be typical of a strong adverse pressure gradient. However, even with substantial increases in the velocity error, the error in the integral quantity, δ^* , remained quite low at 0.121%. As mentioned above, the best potential accuracy available using the hydrogen bubble method is needed for investigating the scalar descriptions of turbulent spots such as δ^* . If the instantaneous velocity calculation yields 3-5% error, the uncertainty of the integral quantity should lower. The value of δ^* for each case was calculated to the y location of the highest bubble for both the marker method and the known profile. The values of δ^* calculated from the trajectory analysis were of the order of the velocity error or less based on the known profile. The accuracy of the integral parameter is a significant benefit provided by the hydrogen bubble wire method in the measurement of turbulent spots.

As mentioned in the introduction, the wake defect is a crucial error source which must be taken into account when using the hydrogen bubble wire method.

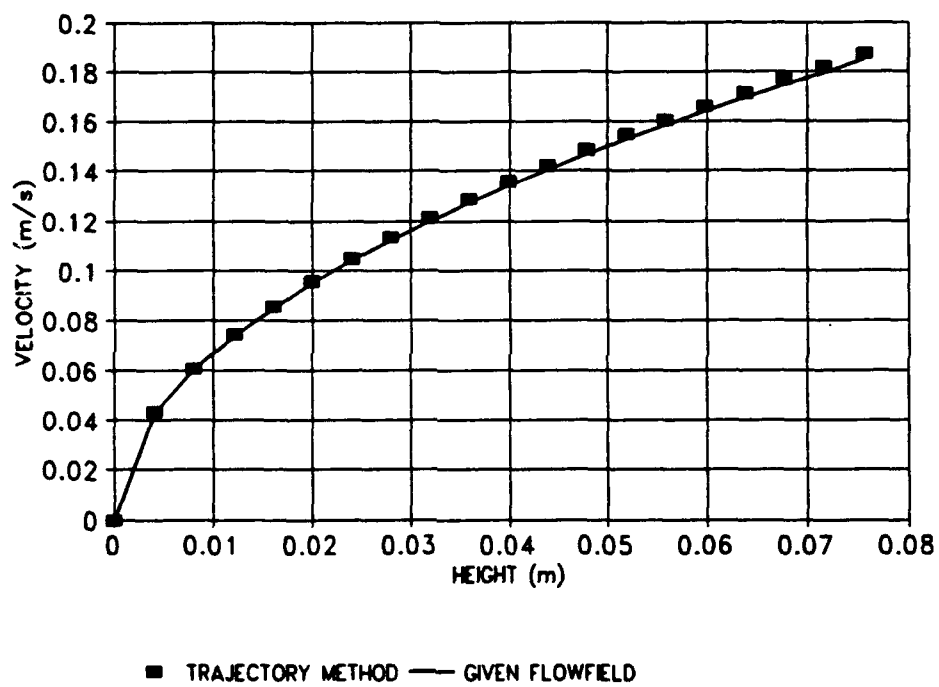


Figure 13. Bubble Trajectory Analysis Case 2.

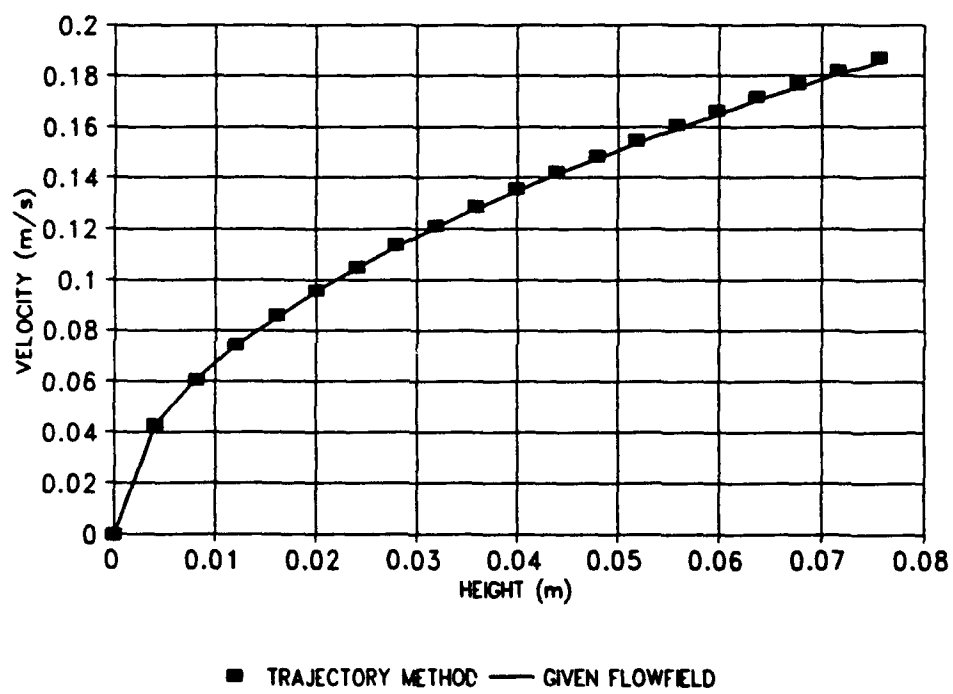


Figure 14. Bubble Trajectory Analysis Case 3.

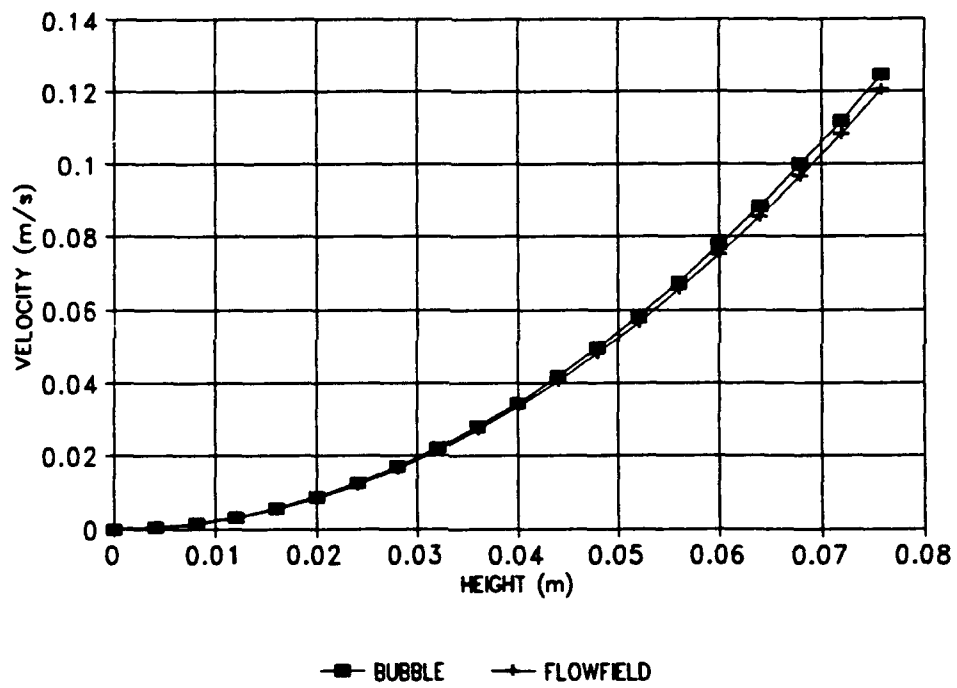


Figure 15. Bubble Trajectory Analysis Case 4.

The major advantage to the hydrogen bubble wire method is that it gives full profile information if it does not obstruct the flow. Lu and Smith (1985) used an extension of a full laminar wake solution to correct for the wire obstruction;

$$\frac{(u-U_b)}{u} = C \left(\frac{x}{d}\right)^{-0.5} \quad (13)$$

where u is the true fluid velocity, U_b is the bubble velocity calculated by the technique, x is the distance of the bubbles from the generating wire, d is the wire diameter, and C is a coefficient which depends on both the local Reynolds number and the wire drag coefficient (Lu and Smith, 1985). Lu and Smith (1987) found that $C = 1.7$ provided a reasonable fit for their data. The present study also found that $C = 1.7$ was a good fit for the data.

3.3. Hydrogen Bubble vs. LDA (Laminar)

After evaluating the hydrogen bubble wire technique using analytical velocity profiles, the method was tested in an actual flow environment. The processing procedure was tested through a wide range of velocities. The experimental apparatus was constrained by limits on some operational parameters, namely voltage, current, and pulse width. Because of these parameters a velocity interval of accuracy needed to be established. This interval was established based on the response of the bubbles to the fluid velocity. Several limitations arose based on the response of the bubbles. In low velocity regions, buoyancy effects predominate. In high velocity regions, bubble clouds exhibit excessive spreading. As bubbles of varying size are created and

swept off of the wire at high speeds, the various sized bubbles are affected in different ways, causing spreading. This spreading contributes to uncertainty in interpreting the edges of the bubble lines. It was found that spreading and buoyancy were the two major limitations in addition to pixel limitations and these limitations served as brackets for the velocity interval.

The low end of the velocity interval was 15 cm/s which was due to the large buoyancy effect near the wall. As described in section 3.2., when the ratio of bubble vertical velocity to mean local fluid velocity near the wall approaches 1/50 there is unacceptable distortion in the profile. Therefore, from the height at which this velocity criteria was met, a curve fit was needed down to the zero slip condition at the wall (section 3.2.1). At a freestream velocity of 15 cm/s, the point at which curve fitting began was approximately 4.5 mm. This height was approximately 12% of the boundary layer. To make the lower end of the interval any lower would entail curve fitting a larger portion of the profile and would therefore limit application of the hydrogen bubble wire method, especially in boundary layer applications. An additional problem arising from a freestream velocity below 15 cm/s was that the buoyancy of the bubbles which formed below 4.5 mm lead to a large scale coalescence of bubbles originating at the base of the wire. This mass of bubbles forced the lower portions of the timelines to group together and "climb." This mass of bubbles was created in the low velocity portion of the boundary layer where the bubble vertical rise rate predominated. Since many bubbles were in this portion of the boundary layer they would each experience substantial vertical rise and group

together until the point in the boundary layer where the local mean velocity dominated the overall velocity vector. In this region the software would calculate zero velocity due to the fact that it was looking for timelines underneath the coalesced mass where no bubbles traveled.

The upper end of the velocity interval was established from the velocity at which the spreading of the timelines did not hinder the software from establishing a definitive edge. Using 95 volts and 130 mA throughout the study provided sufficiently dense bubble clouds from 15 cm/s to 22.22 cm/s. As mentioned in the experimental descriptions, the pulse width within the experimental control software could be adjusted from 1 to 10 ms. Variations could be seen as pulse width changed at the lower velocities. However, the results were not linear, i.e., an 8 ms pulse width would not yield a cloud twice as wide as a 4 ms pulse width. The width would change slightly while it was observed that the density of the bubble clouds changed dramatically. With this result and the electrical pulse limited to 95 volts and 130 mA, the pulse width was increased with increasing speed in order to make the bubble clouds more dense and less sensitive to spreading. Above 22.22 cm/s, however, the combination of voltage and current available to produce hydrogen gas at the wire was essentially exhausted as the spreading could not be overcome by increasing the pulse width. The spreading of the bubbles in the freestream lead to severe lighting non-uniformity as bubbles of varying size were exposed to varying buoyant and shear forces, even with the pulse width at 10 ms. In order to overcome this, the next step would be to increase the voltage and/or the current. With the present voltage limits,

the technique is effectively limited to a range of 15 cm/s to 22.2 cm/s.

The camera field of view was set based on the expected size needed for measuring unsteady turbulent spot velocity profiles. With the field of view sufficiently large to capture the full height of a turbulent spot passage, the pixel resolution for all of the cases studied yielded a y scale of 0.012 cm/pixel and an x scale of 0.016 cm/s, which is an aspect ratio x/y of 4/3. The spacing of the timelines ranged from 32 pixels between timelines at 15 cm/s to 48 pixels between timelines at 22.22 cm/s.

LDA surveys at each speed were completed using 30 y locations and averaging over 30 seconds. Instantaneous and time-averaged hydrogen bubble velocity profiles are compared to the LDA surveys. Typical instantaneous hydrogen bubble profiles for 15 cm/s, 18.9 cm/s, and 22.22 cm/s are shown in figures 16-18. As a supplementary procedure to further substantiate the assumption that the Eulerian field velocity equals the Lagrangian time-average velocity (section 3.2.1.) the laminar speeds were tested with two pulse intervals. Figures 16-18 had a time between pulses at 1/30 second. The second tests had a pulse interval of 1/15 second which increased the distance between the timelines. The results are shown in figures 19-21. The results of the $t = 1/30$ second tests yielded freestream velocity errors of approximately $\pm 5\%$ and errors of $\pm 1\%$ near the wall. With $t = 1/15$ second the freestream velocity error remained about the same although the freestream velocities tended to be higher than the LDA results rather than straddling the LDA measurements as in the latter case.

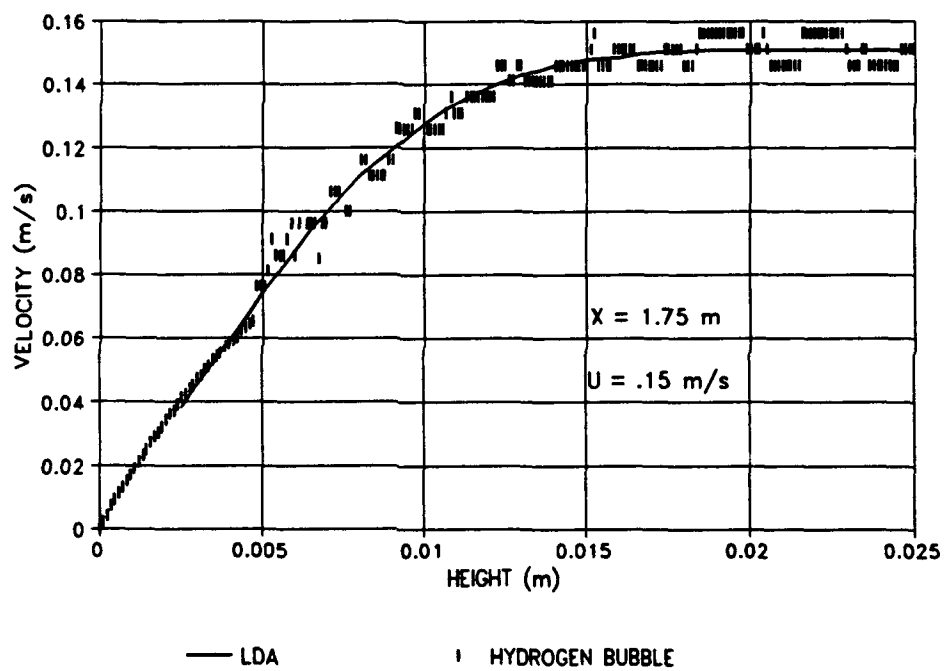


Figure 16. Instantaneous Hydrogen Bubble vs. LDA (15 cm/s, $t = 1/30$ sec)

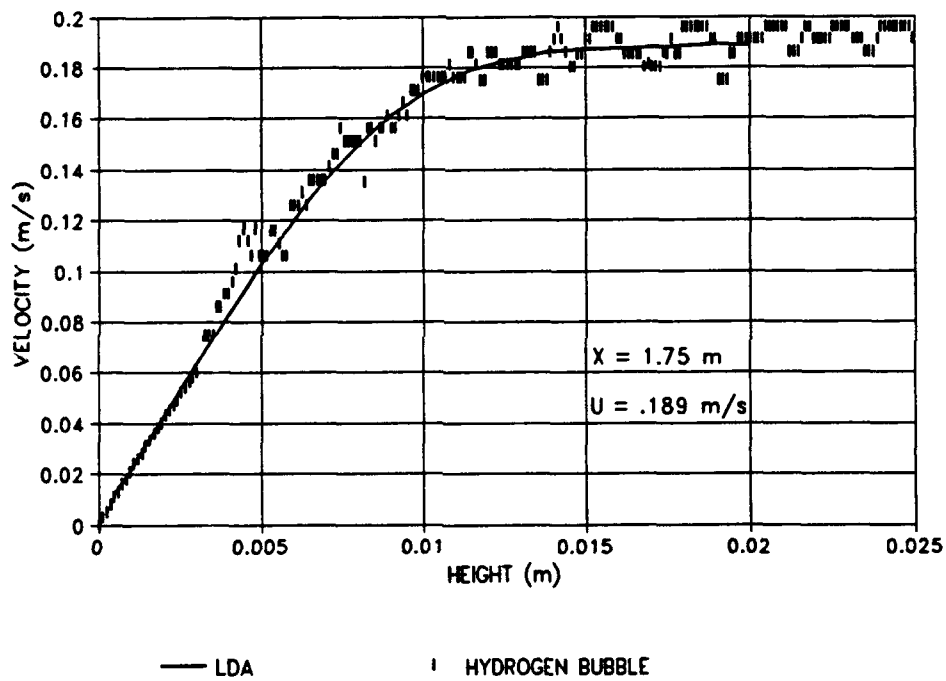


Figure 17. Instantaneous Hydrogen Bubble vs. LDA (18.9 cm/s, $t = 1/30$ sec).

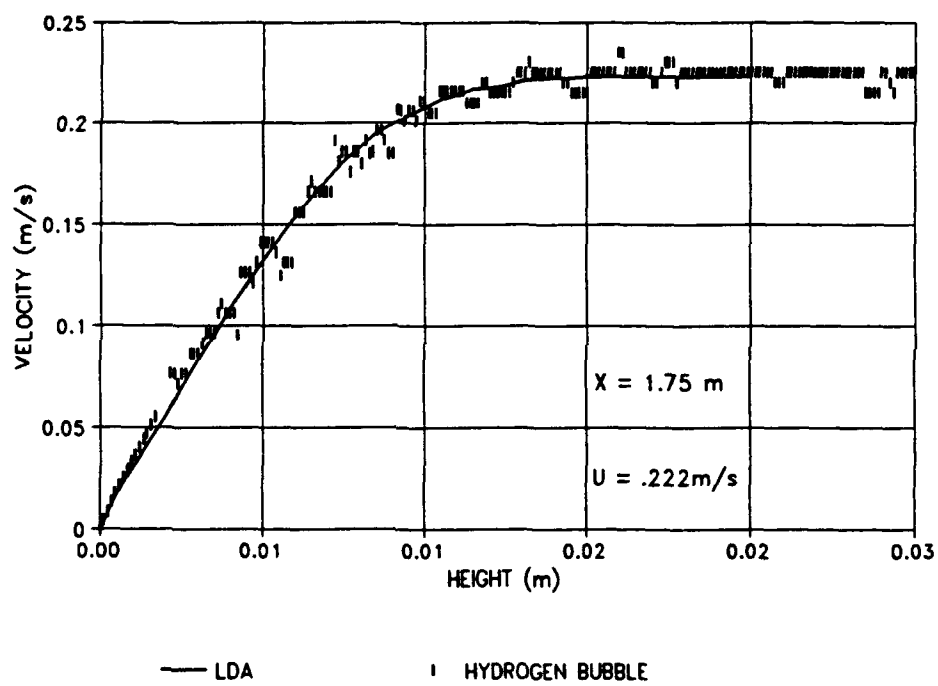


Figure 18 . Instantaneous Hydrogen Bubble vs. LDA (22.22 cm/s, $t = 1/30 \text{ sec}$).

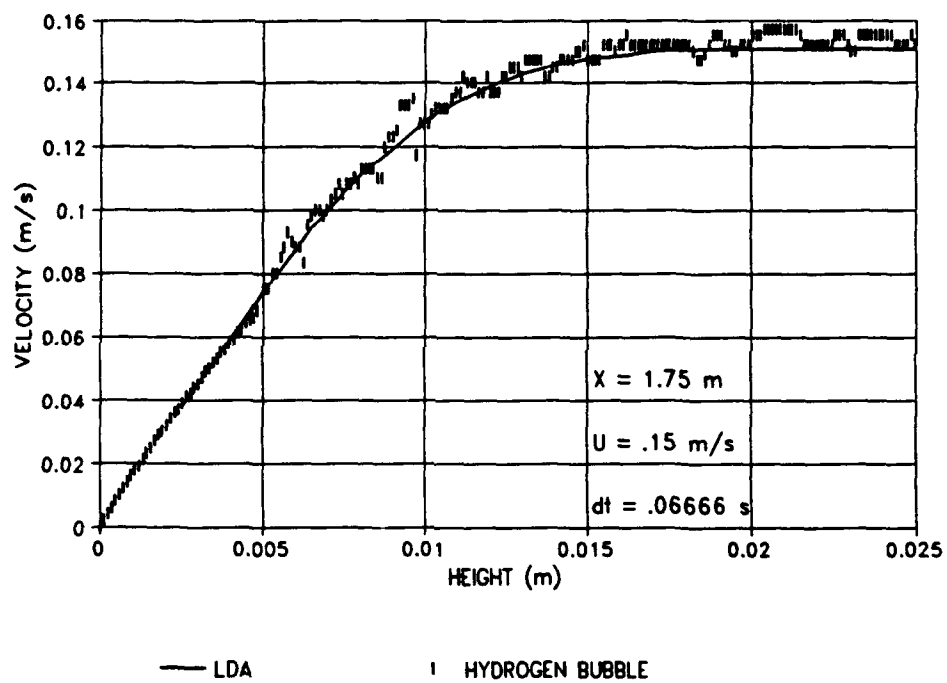


Figure 19. Instantaneous Hydrogen Bubble vs. LDA (15 cm/s, and $t = 1/15$ sec).

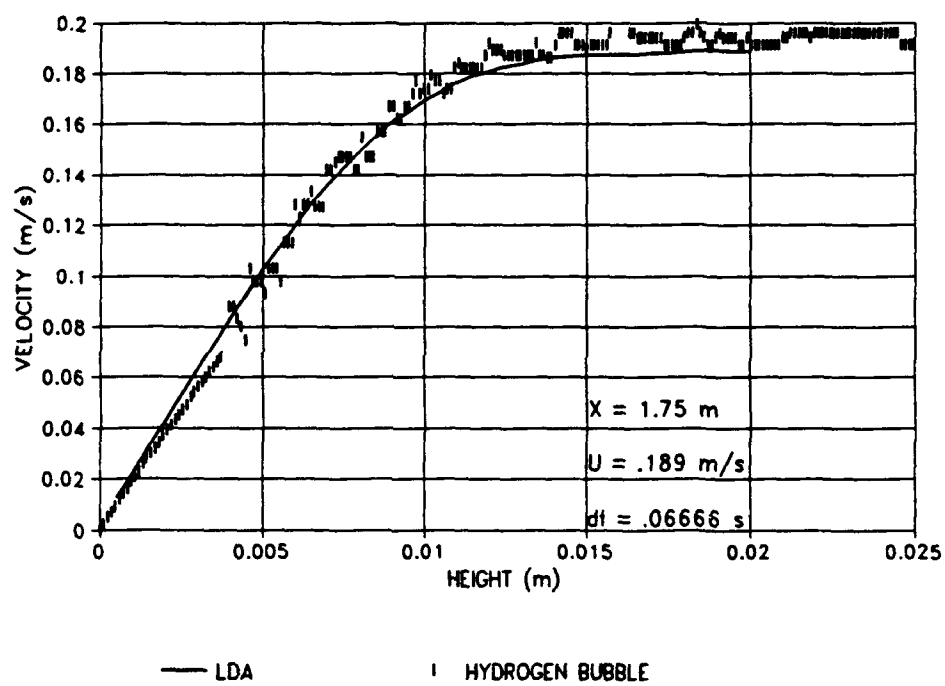


Figure 20. Instantaneous Hydrogen Bubble vs. LDA (18.9 cm/s, $t = 1/15$ sec).

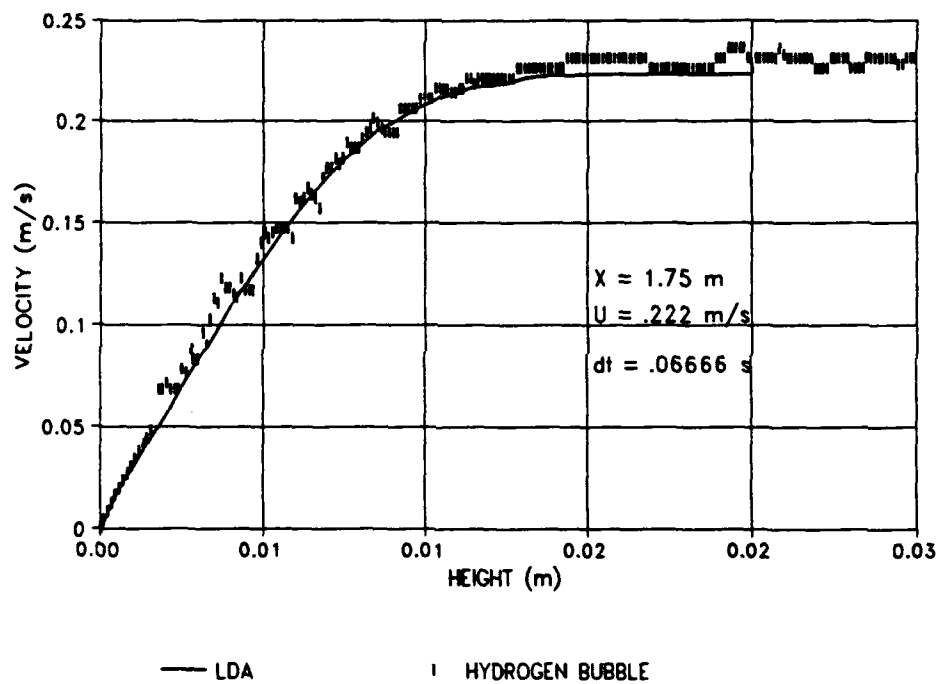


Figure 21. Instantaneous Hydrogen Bubble vs. LDA (22.22 cm/s, $t = 1/15$ sec).

Time averaging of the results improved the percent error for all test velocities between the two procedures. As can be seen from figures 22-27, the two techniques vary only slightly. All but the 22.22 cm/s case with $t = 1/15$ second agree well. This latter case suffered from severe spreading as the high speeds and long times of travel magnified the effects of spreading.

Important for the work with turbulent spots, the accuracy of the integral parameters was investigated. Figures 28-33 show the comparison of integral parameters between the two methods. The results are fairly good for most of the time-averaged values. However, the cases have a rather high rms around the respective means of 10-15%. The best case was at 18.9 cm/s, which was expected as the velocity profile error was optimal at this speed as well. It is interesting to note in all of the plots that the rms is rather high, approximately 1-10%, but certain speeds and time intervals yielded spikes in the results. In a laminar flow the integral parameters should remain constant. The spikes could be due to non-uniform bubble production, debris in the flow which would confuse the software, or the curve fit down by the wall misinterpreting boundary conditions. As evident by the integral parameter vs. time results at 18.9 cm/s, this speed yielded the least error and was the best choice of velocity for making the turbulent spot measurements.

The laminar tests were performed to establish the accuracy of the method and to obtain a velocity range for applicability of this hydrogen bubble wire method to boundary layers. The final goal was to establish the velocity at which the image processing software would provide optimum results. This velocity was 18.9 cm/s.

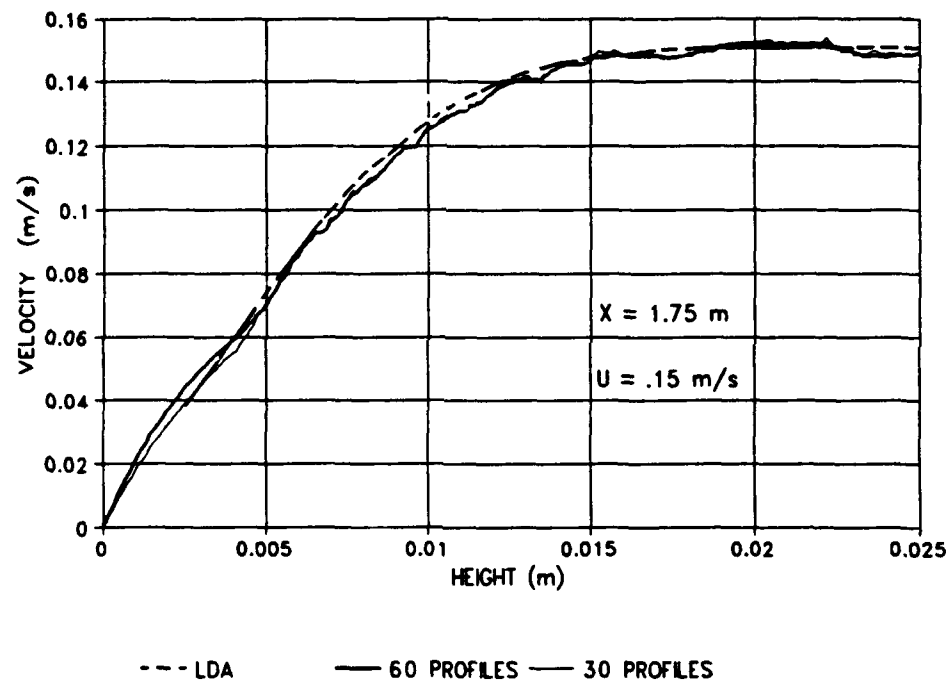


Figure 22 . Time-Averaged Hydrogen Bubble vs. LDA (15 cm/s, t=1/30 sec).

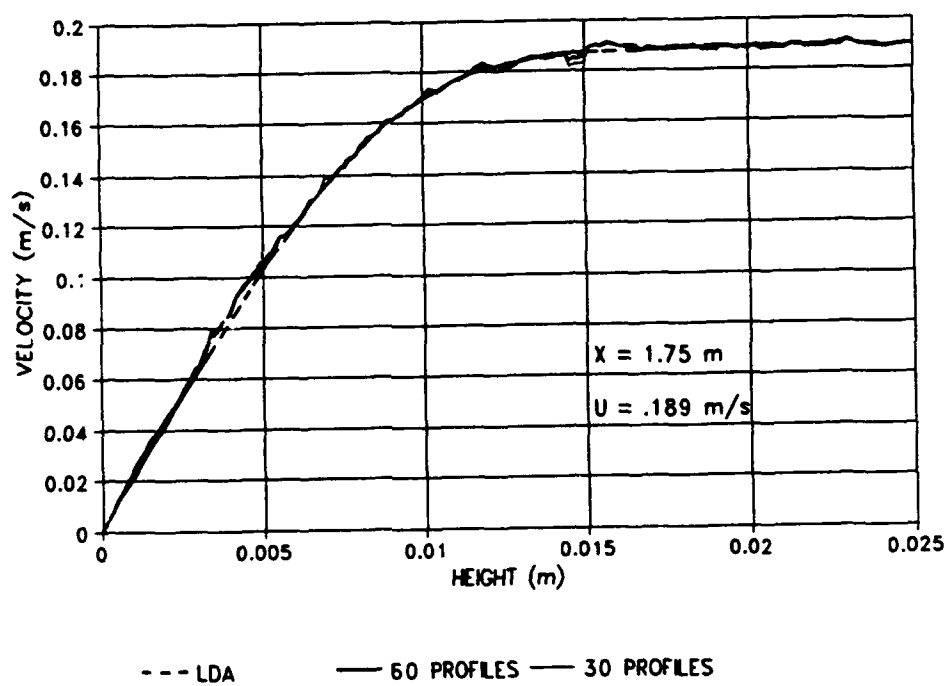


Figure 23. Time-Averaged Hydrogen Bubble vs. LDA (18.9 cm/s, $t=1/30$ sec).

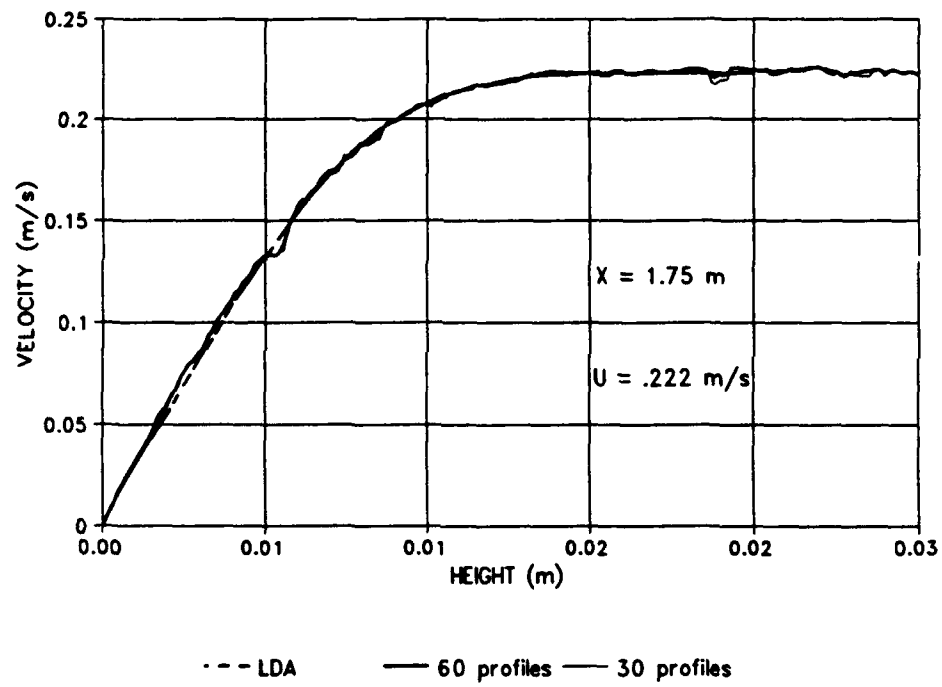


Figure 24. Time-Averaged Hydrogen Bubble vs. LDA (22.22 cm/s, $t=1/30$ sec).

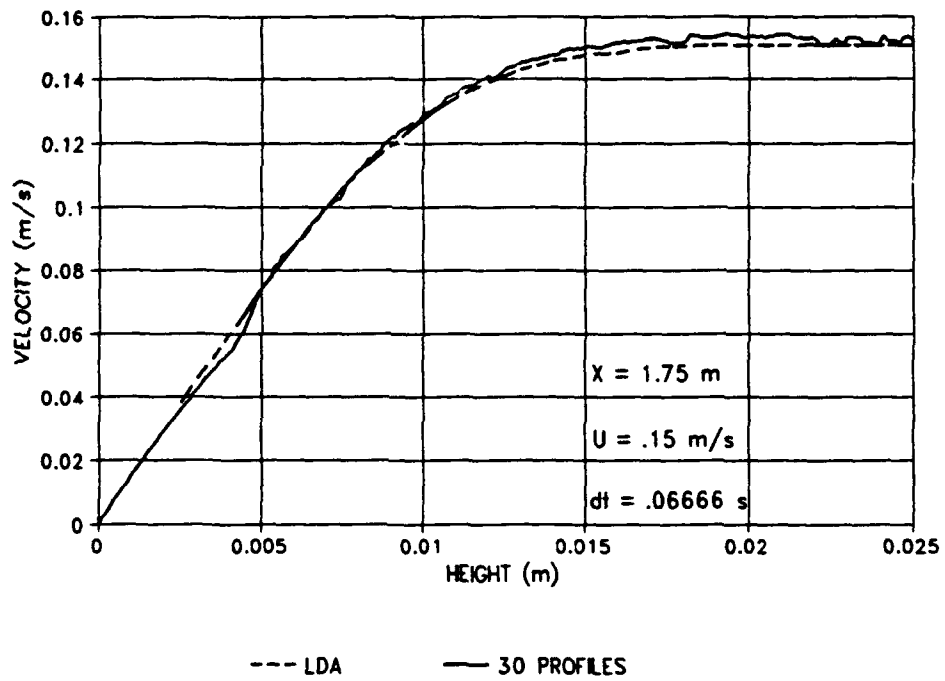


Figure 25. Time-Averaged Hydrogen Bubble vs. LDA (15 cm/s, $t = 1/15$ sec).

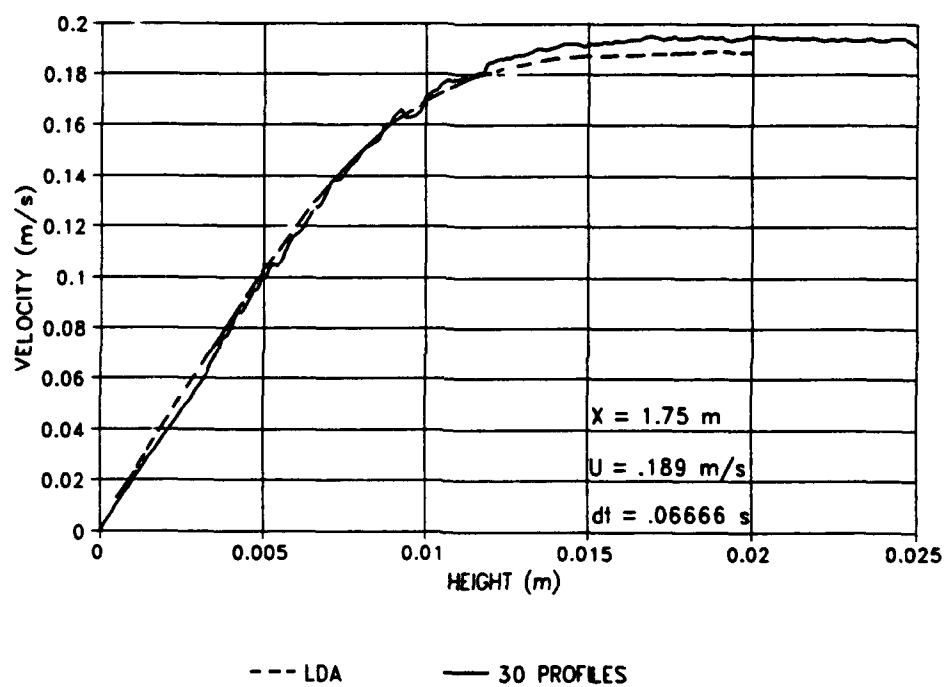


Figure 26. Time-Averaged Hydrogen Bubble vs. LDA (18.9 cm/s, $t = 1/15$ sec).

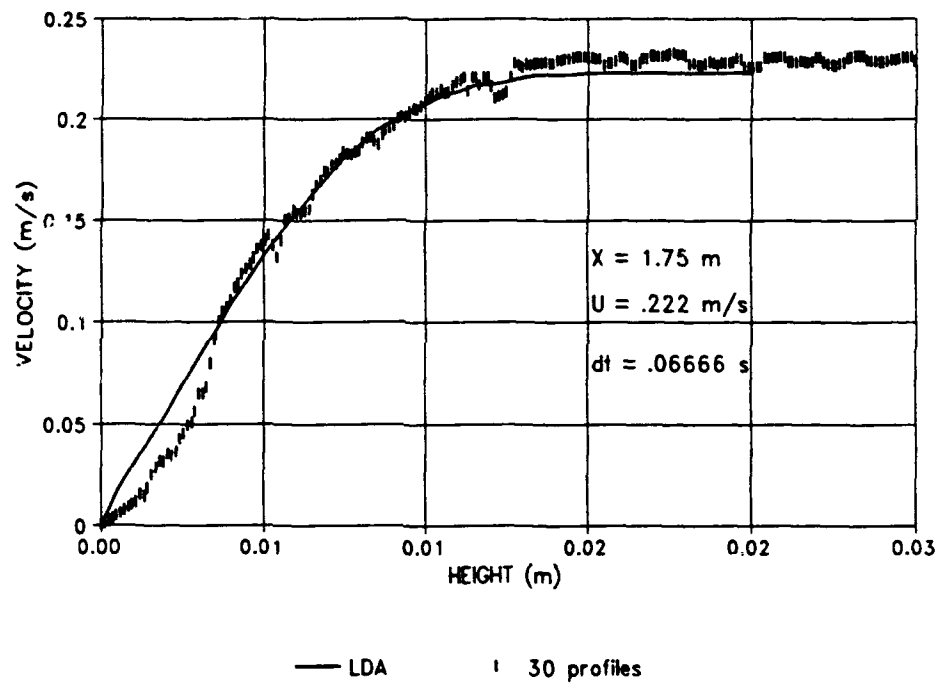


Figure 27. Time-Averaged Hydrogen Bubble vs. LDA (22.22 cm/s, $t = 1/15$ sec).

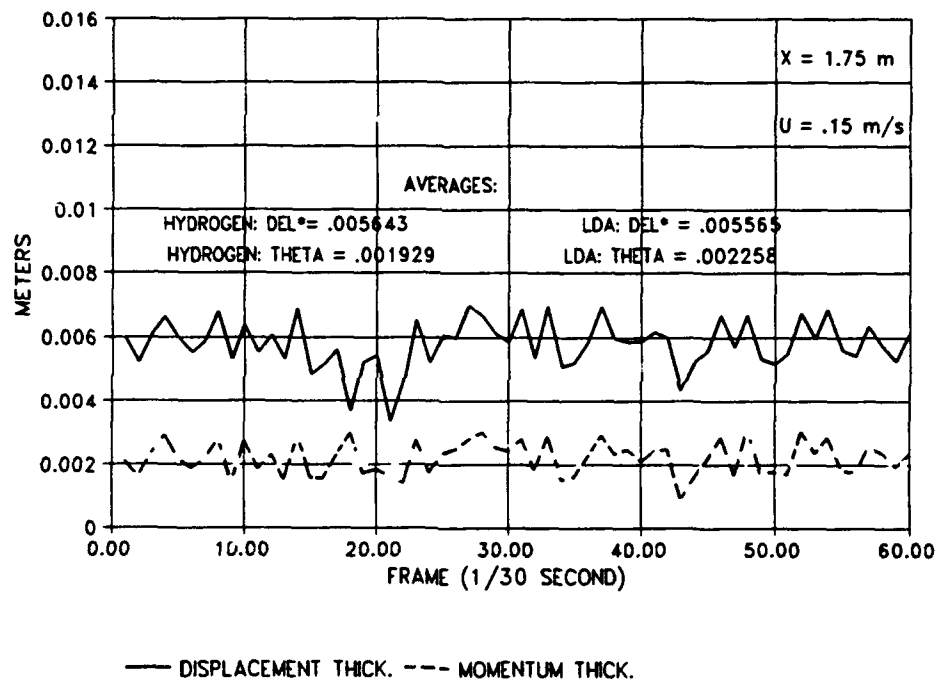
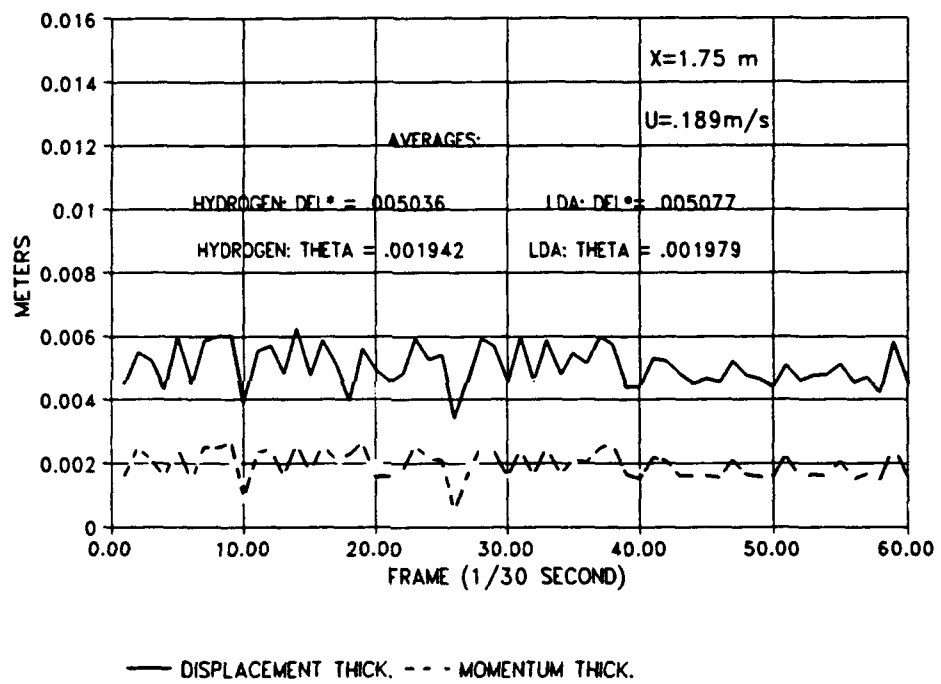


Figure 28. Hydrogen Bubble Integral Parameters vs. Time
 (15 cm/s, $t = 1/30$ sec).



**Figure 29. Hydrogen Bubble Integral Parameters vs Time
(18.9 cm/s, $t = 1/30$ sec).**

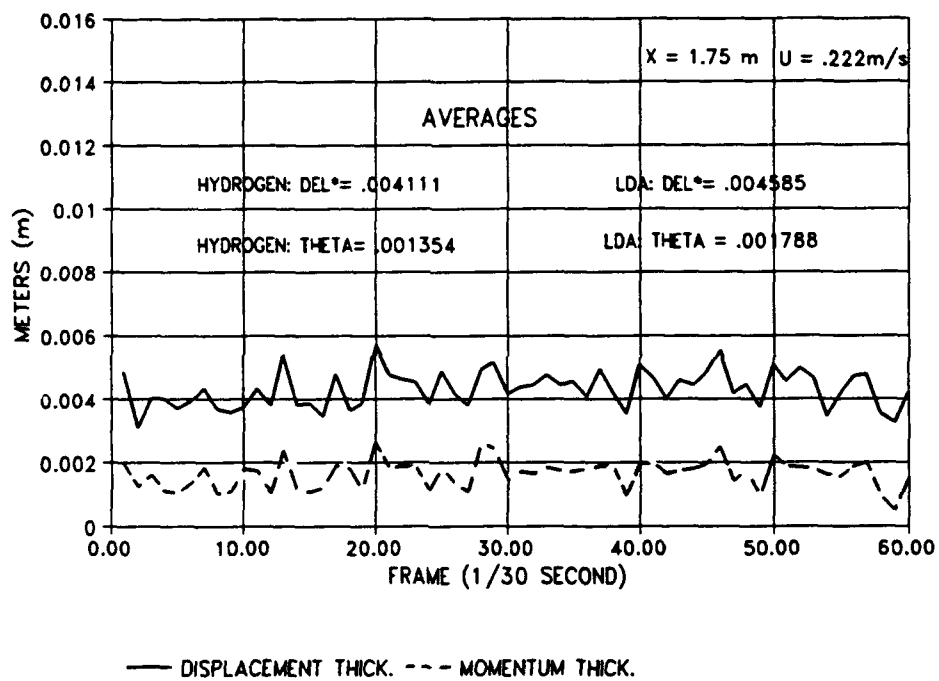


Figure 30. Hydrogen Bubble Integral Parameters vs. Time
 (22.22 cm/s, $t = 1/30$ sec).

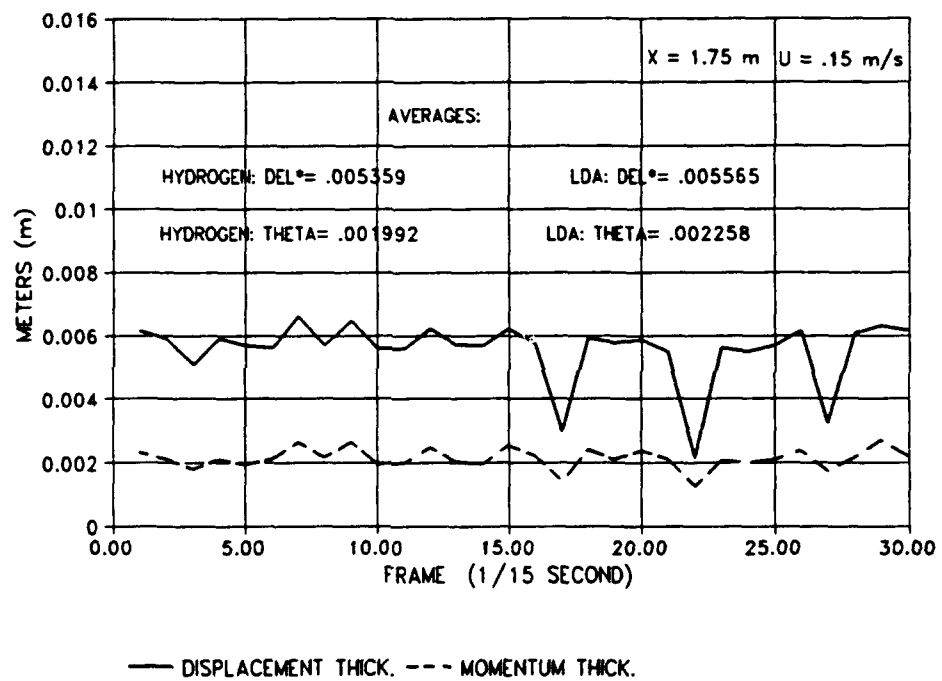


Figure 31. Hydrogen Bubble Integral Parameters vs. Time
 (15 cm/s, $t = 1/15$ sec).

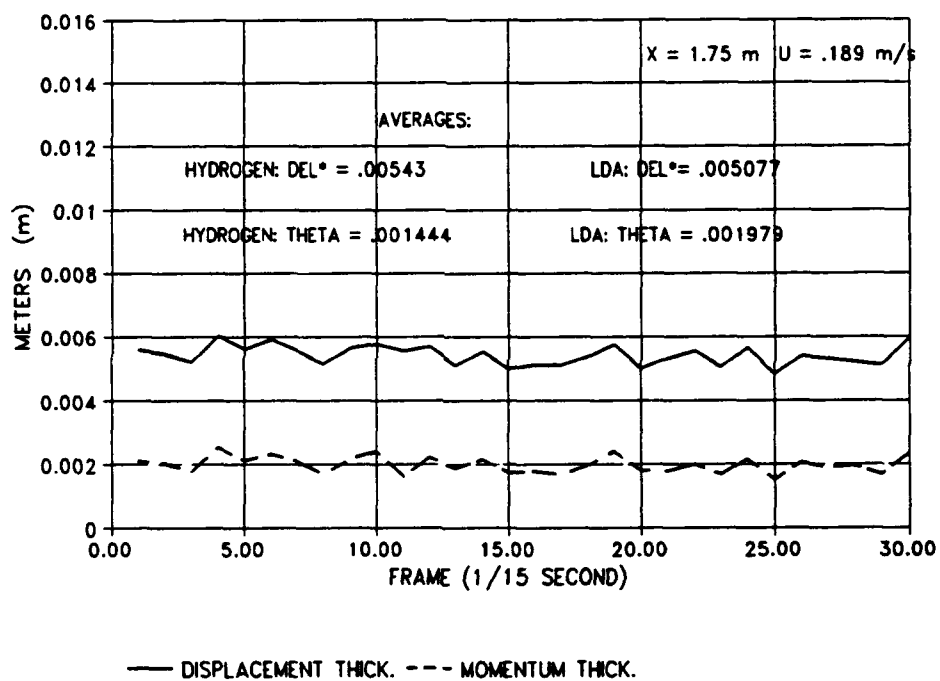


Figure 32. Hydrogen Bubble Integral Parameters vs. Time
 (18.9 cm/s, $t = 1/15 \text{ sec}$).

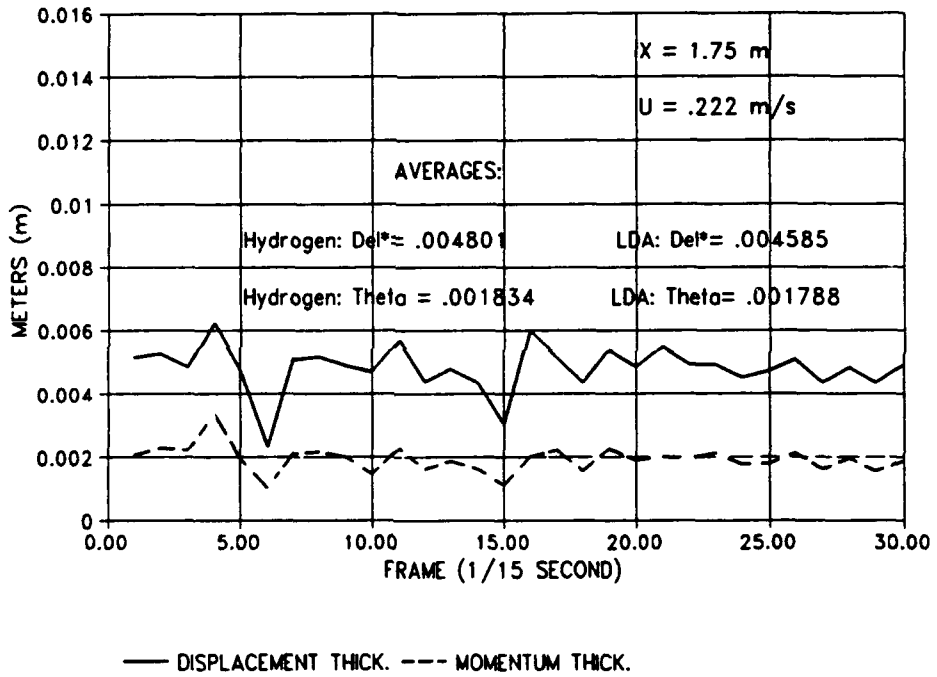


Figure 33. Hydrogen Bubble Integral Parameters vs. Time
(22.22 cm/s, t = 1/15 sec).

It must also be noted that finding the wall for both the hydrogen bubble method and the LDA is subject to errors as well. For the LDA the error could be from one to two probe volumes and the hydrogen bubble error could be from one to two pixels (1 pixel = 0.012 cm). Figure 34 exemplifies how shifting the wall pixel by two affects the hydrogen bubble results with respect to the LDA. The velocity profiles in figure 34 are five profile averages at 18.9 cm/s. Notice that the difference is minimal throughout the profile.

3.4. Hydrogen Bubble vs. LDA (Turbulent Spots)

The passing of a turbulent spot is a transient event. Velocity profiles vary from laminar to turbulent and back to laminar. In the experimental setup, the hydrogen bubbles tracking the flow encountered various velocity gradients. Because of these various gradients, the application of the hydrogen bubble method to the turbulent spot took several iterations.

The 1/50th criteria for curve fitting down to the wall was first attempted on each and every timeline within the spot passing. This method proved to be quite erroneous as certain deformed profiles gave the 1/50th criteria at various y locations within the region of interest, and other profiles would not yield the criteria until very close by the wall where the lighting failed the method. The processing procedure was then adjusted to curve fit from a set height for each and every profile. The height was chosen based on the 1/50th criteria that the laminar profiles encountered. This location occurred just above the height where the lighting became too dim for

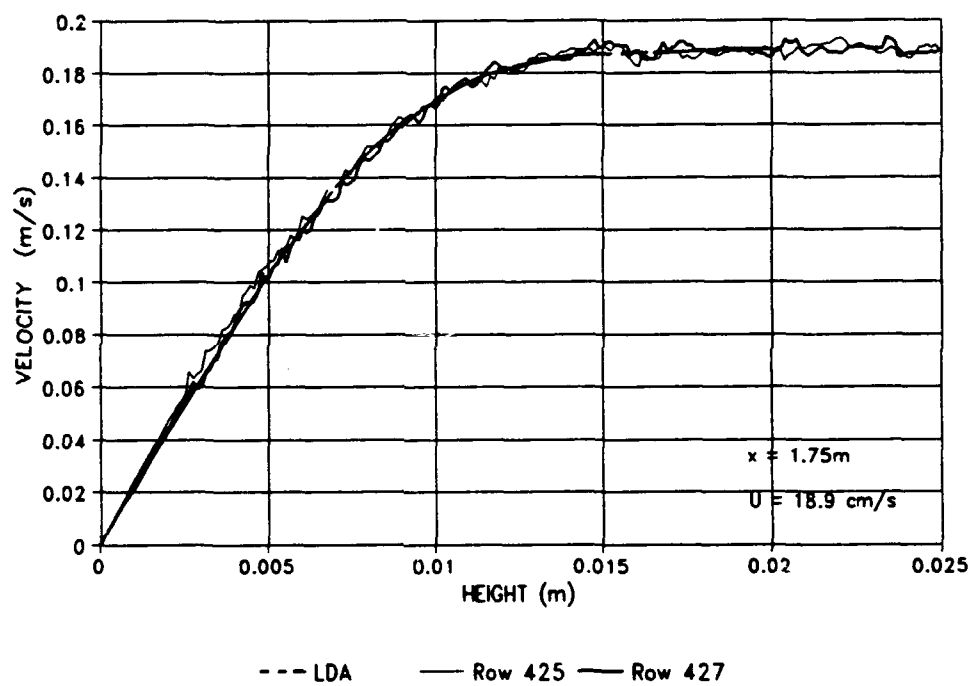


Figure 34. The Effects on the Velocity Profile by Shifting the Wall Pixel by Two.

the software to recognize a timeline edge. This y location was about 2.5 mm. Since the region of interest stretched to 3.65 cm, the curve-fit area made up only 6.8% of the entire profile.

The goal of the hydrogen bubble wire method with respect to turbulent spots was to obtain instantaneous δ^* vs. time traces for individual spot realizations. Out of the three speeds in the velocity interval, the freestream velocity of 18.9 cm/s yielded the least error in the δ^* calculation. However, the turbulence intensity at this speed was approximately 0.5%. By increasing the velocity to 19.04 cm/s, the turbulence intensity came down to 0.3% and this was more suitable for the experiments. Furthermore, obtaining a centerline realization of the spot could only be done at the centerline port at $x = 1.75$ m from the leading edge. At this location, a freestream velocity of 19.04 cm/s was the maximum speed at which tests could be run without the effects of sidewall contamination.

Thirty spots were videotaped and processed. The processing time was substantial due to the manual frame advance. In order to keep the post-processing time to a minimum, the experimental control was set to begin pulsing six seconds after the spot was generated and end approximately 8.5 seconds later. This time interval covered only the most dynamic area of the spot passing. The duration of the entire spot passage was about 25 seconds from laminar profile back to laminar profile. This processing time included 250 frames per spot at 1/30 of a second apart for a total of 7500 frames.

The LDA data was obtained by generating 40 spots while the probe was

positioned at each of 22 y locations. This procedure yielded a total of 880 spots generated and analyzed. The processing was done by first ensemble averaging each $u(y,t)$ and then obtaining the δ^* from the ensemble averaged profile. The hydrogen bubble method calculated instantaneous δ^* at each 1/30th of a second which were then ensemble-averaged. The realization of 30 ensemble-averaged hydrogen bubble results show very good agreement with the LDA measurements, figure 35. Two regions of direct interest are at $t = 7.6$ seconds and $t = 9.75$ seconds. Position 1 at $t = 7.6$ seconds shows an upward trend in the hydrogen bubble results while the LDA shows a downward trend. Position 2 at $t = 9.75$ seconds shows that the hydrogen bubble method yielded a higher value of maximum δ^* . Inspection of the ensemble-averaged velocity profiles from the two methods at these times explains the discrepancy (figures 36 and 37). From the comparison of the two velocity profiles in each figure, it is evident that the hydrogen bubble method is very susceptible to the severe gradients within the spots. The timelines retain their bubble density and do not experience the spreading effect detailed in section 3.3. Figures 38 and 39 show the severe deformation of the timelines which results in the severely distorted velocity profiles. Figures 38a and 39a are laminar flow timelines to compare with the remaining video images. The remaining five images are sequential video images from the times noted for spot #1. In each case, there is non-uniform distance between the timelines from the freestream to the wall. this non-uniformity in ΔX is the direct reason for the distortion in the velocity profiles. The likely problem at these two locations is the averaging effects that arise due to the time-averaged

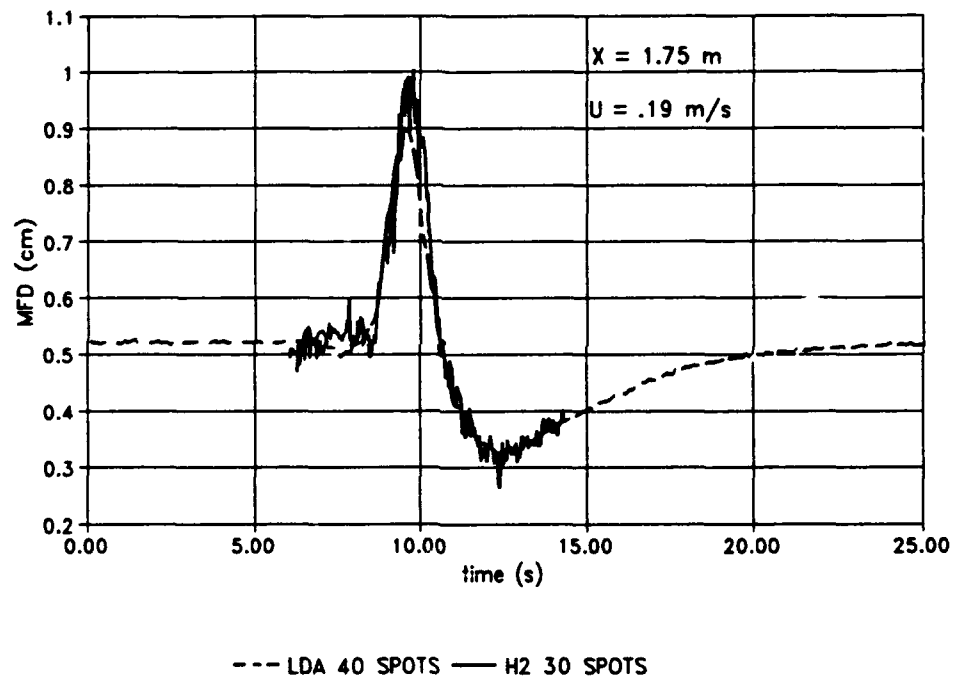


Figure 35. Ensemble-Averaged δ^* vs. Time for Hydrogen Bubble and LDA.

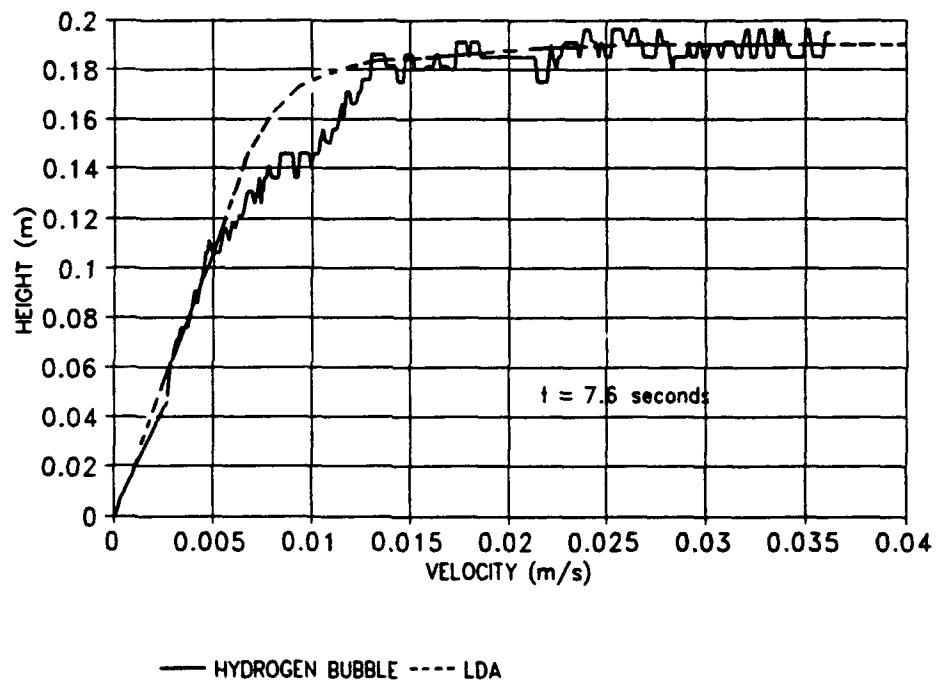


Figure 36. Hydrogen Bubble and LDA Ensemble-Averaged Velocity Profiles at $t = 7.6$ seconds.

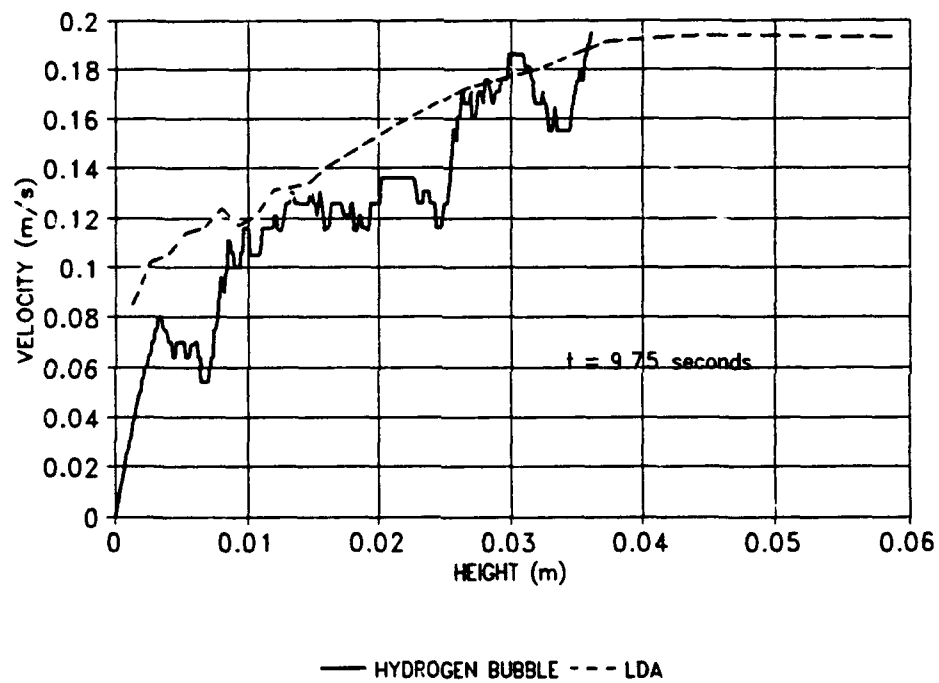


Figure 37 Hydrogen Bubble and LDA Ensemble-Averaged Velocity Profiles at $t = 9.75$ seconds.

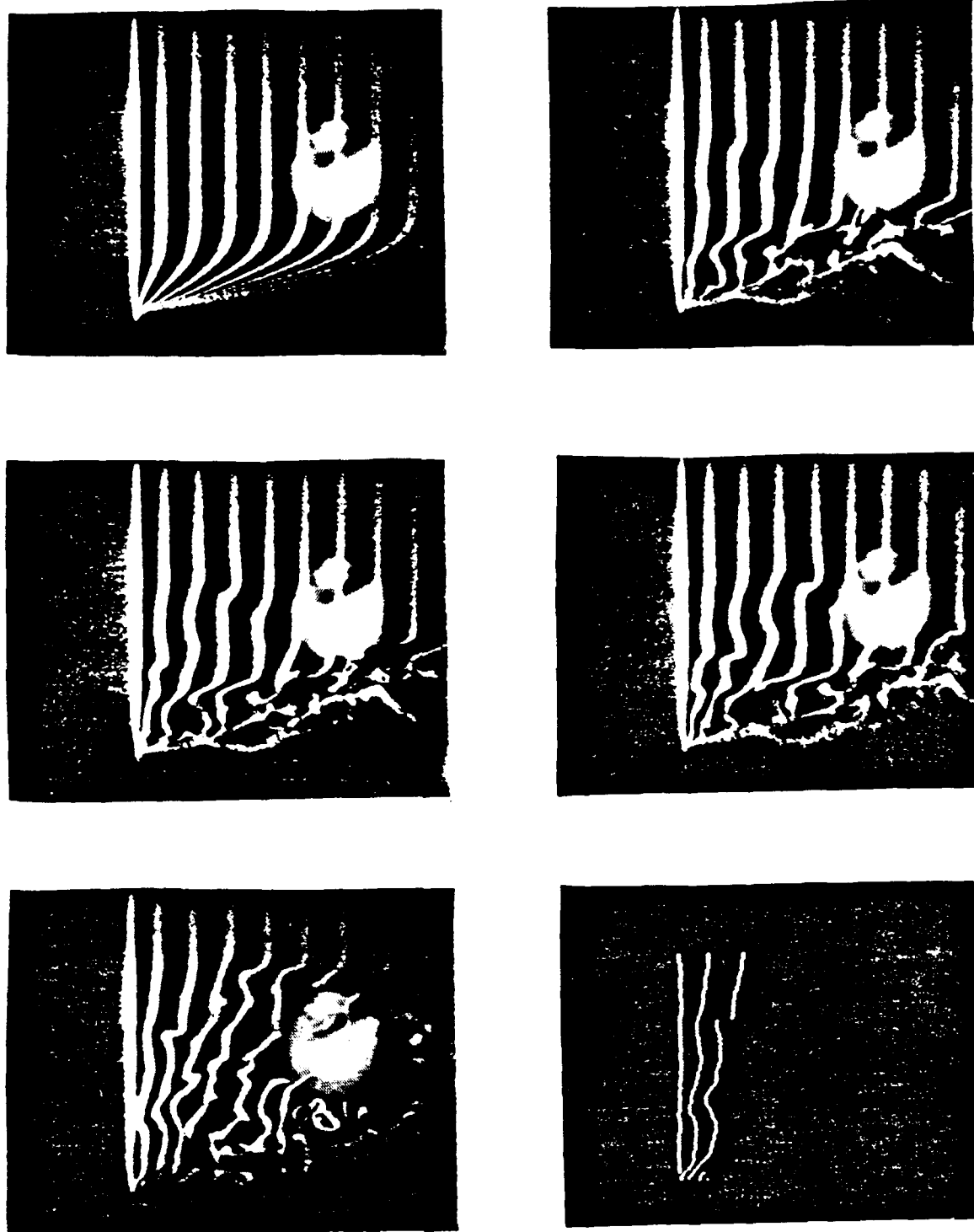


Figure 38. Actual Video Frames from Turbulent Spot Passing: a) Laminar Flow Timelines for Comparison with times at b) 7.53334 c) 7.56667 d) 7.6000 e) 7.63333 f) Processed Image at 7.63333 sec.

AD-A236 392

DIGITAL IMAGE PROCESSING OF HYDROGEN BUBBLE LINES FOR
INSTANTANEOUS VELOCITY PROFILES (U) PENNSYLVANIA STATE
UNIV UNIVERSITY PARK APPLIED RESEARCH LA.

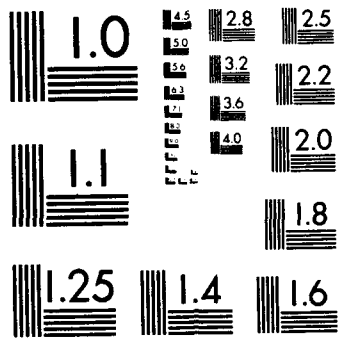
UNCLASSIFIED

S D BRURIEAU ET AL. NOV 92 PSU/ARL-TR-92-10

NL

10	14
12	16
18	22

END
FILMED
DTIC



RESOLUTION TEST CHART
1963-A

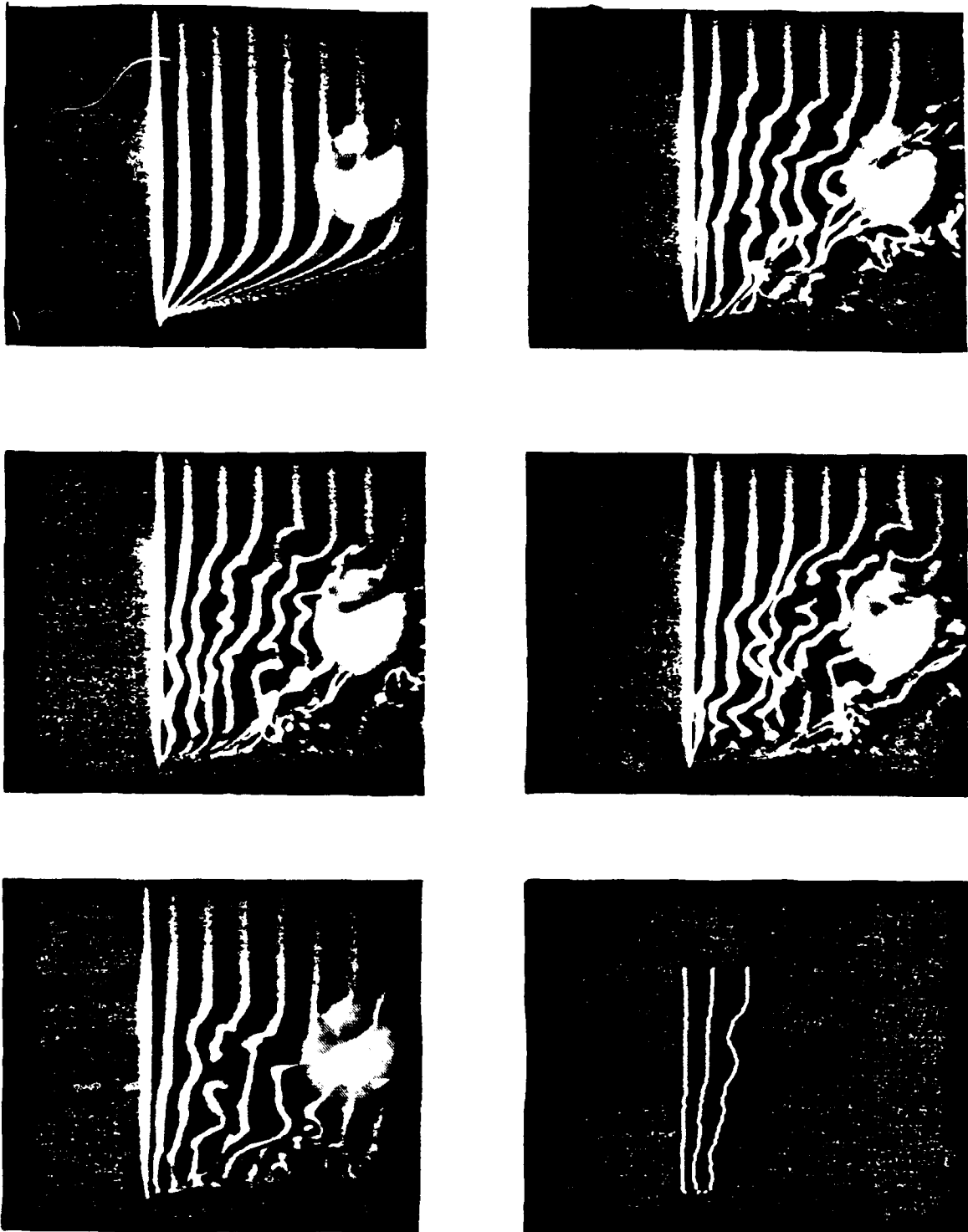


Figure 39. Actual Video Frames from Turbulent Spot Passing: a) Laminar Flow Timelines for Comparison, with times at b) 9.73332 c) 9.76665 d) 9.79998 e) 9.83331 f) Processed Image at 9.83331 sec.

Lagrangian velocity of the bubbles. However, this hypothesis can not be substantiated since the two results were obtained in two very different ways. Ensemble-averaging can predict the overall scales of the flowfield but fails to yield information about the substructures within. In order to obtain a definitive analysis of the difference in results, a second technique to measure instantaneous velocities would need to be developed for comparison with the hydrogen bubble method.

Investigation of the instantaneous traces of δ^* from the hydrogen bubble method versus the LDA ensemble average result shows that each spot not only follows the overall scales described by the averaged results but also the individuality of each spot (figures 40-46). It is evident that there is a histogram of peaks, arrival times, periods, and sharpness. The data in these plots is raw data and has not been filtered in any way. Each spot has substantial noise throughout the realization; however it was found that for the 18.9 cm/s laminar case, the rms about the mean δ^* value was approximately twelve percent. The rms in each of the instantaneous traces seems to be greater than twelve percent.

It is uncertain at the time of this study whether the fluctuations in the hydrogen bubble results are due only to the error in the technique or if the fluctuations are also describing the substructures within the spot. Again, the only way of making a definitive statement about the fluctuations is by direct comparison of results obtained with another instantaneous technique. The error in the method itself is, no doubt, a substantial contributor to the rms in the signal but the question of how much of a contributor arises. Clearly these results suggest that the practice

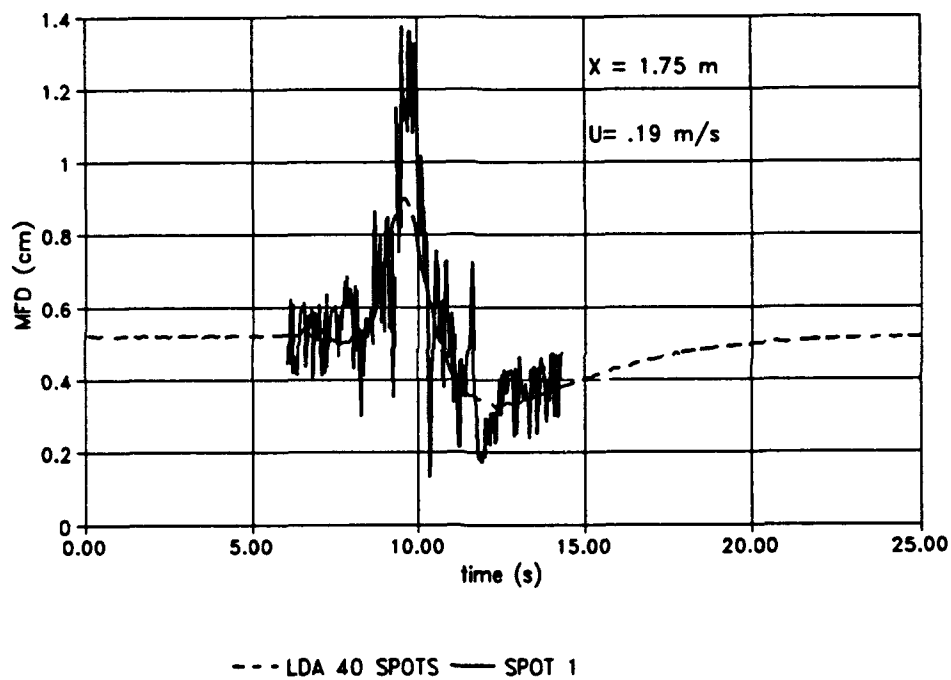


Figure 40. Hydrogen Bubble Instantaneous δ^* vs. Time Spot #1.

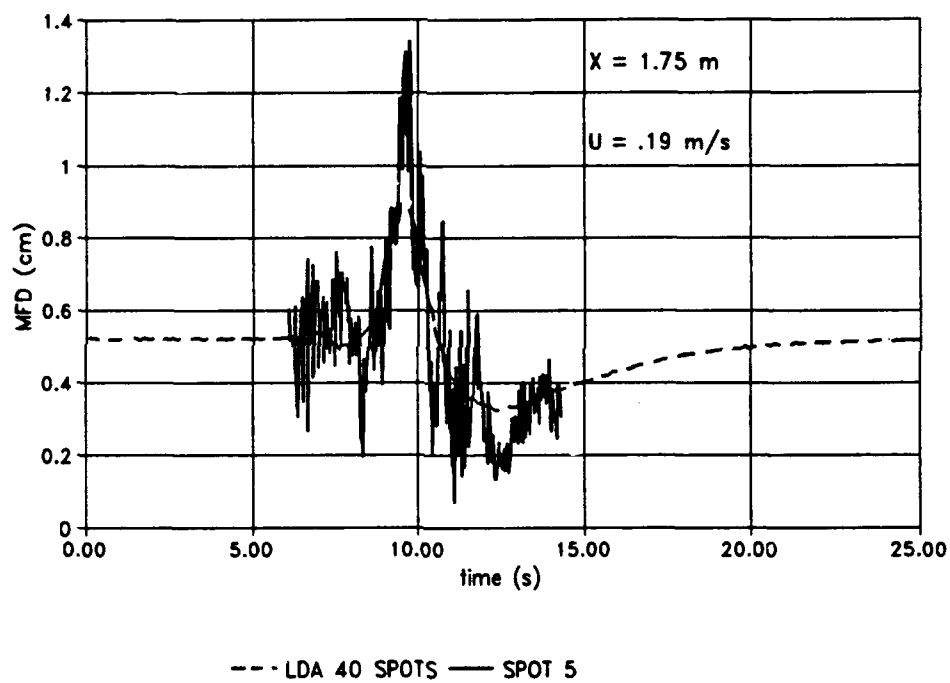


Figure 41. Hydrogen Bubble Instantaneous δ^* vs. Time Spot #5.

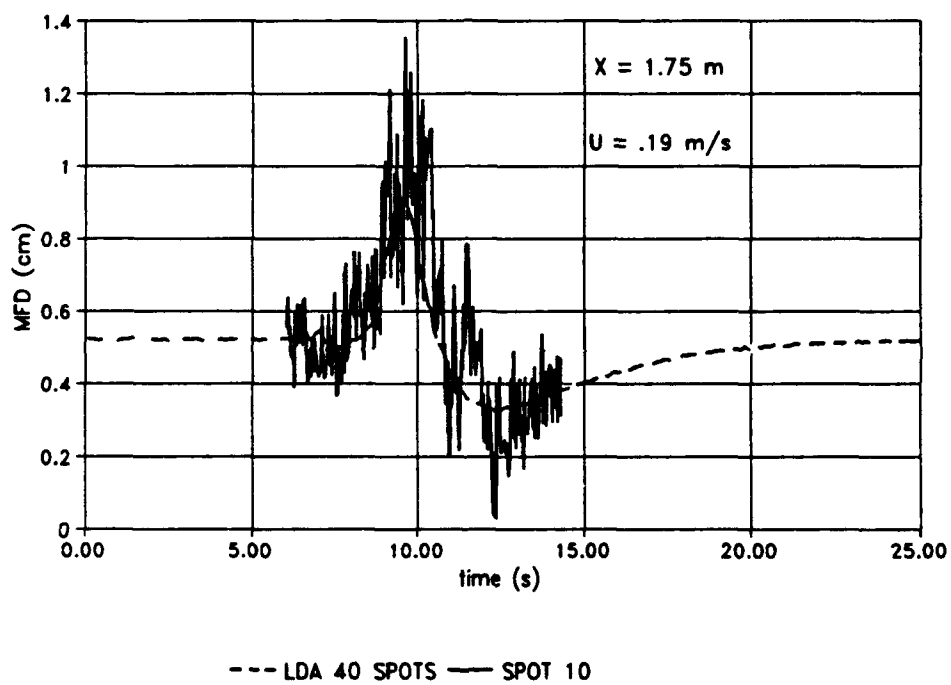


Figure 42 . Hydrogen Bubble Instantaneous δ^* vs. Time Spot #10.

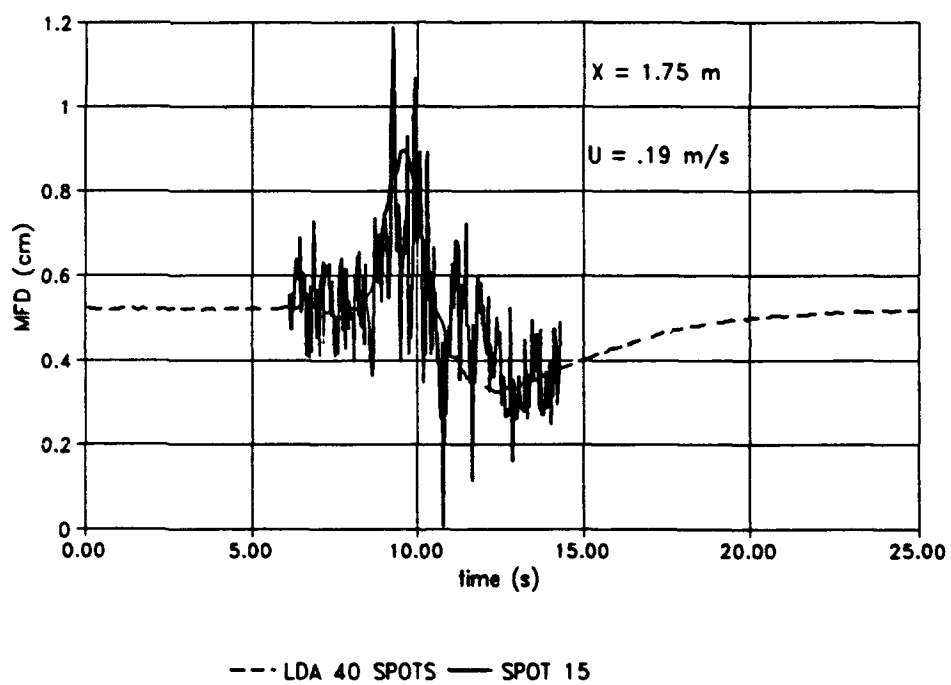


Figure 43. Hydrogen Bubble Instantaneous δ^* vs. Time Spot #15.

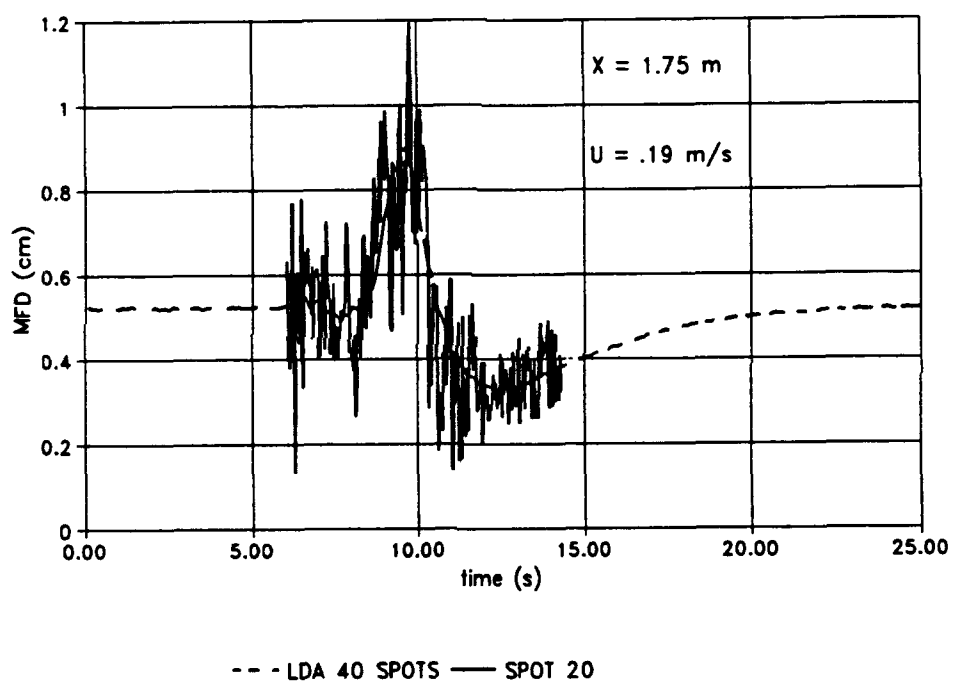


Figure 44 . Hydrogen Bubble Instantaneous δ^* vs. Time Spot #20.

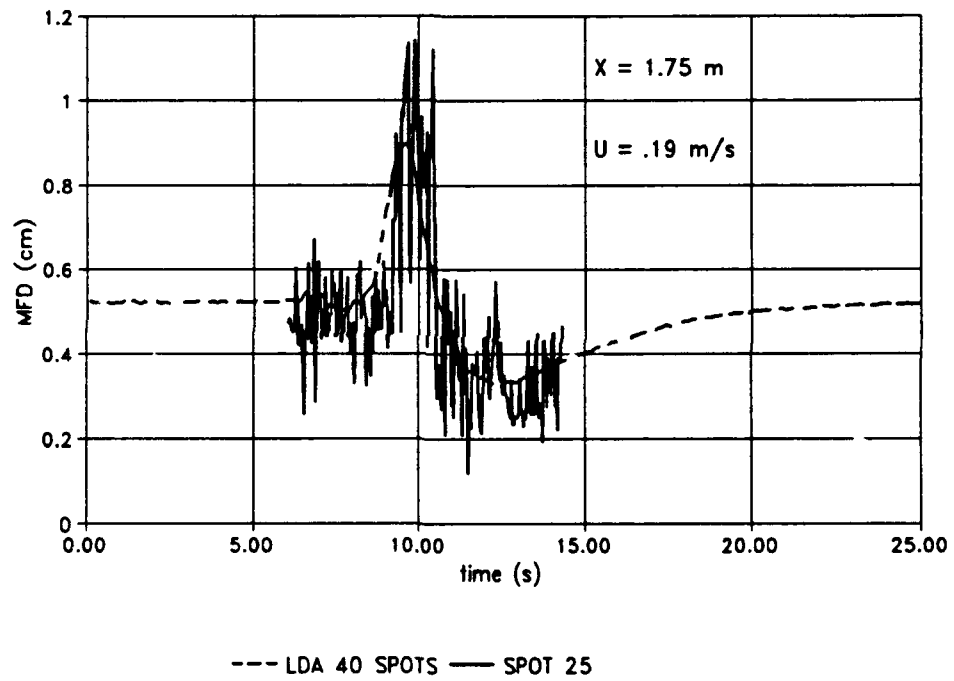


Figure 45. Hydrogen Bubble Instantaneous δ^* vs. Time Spot #25.

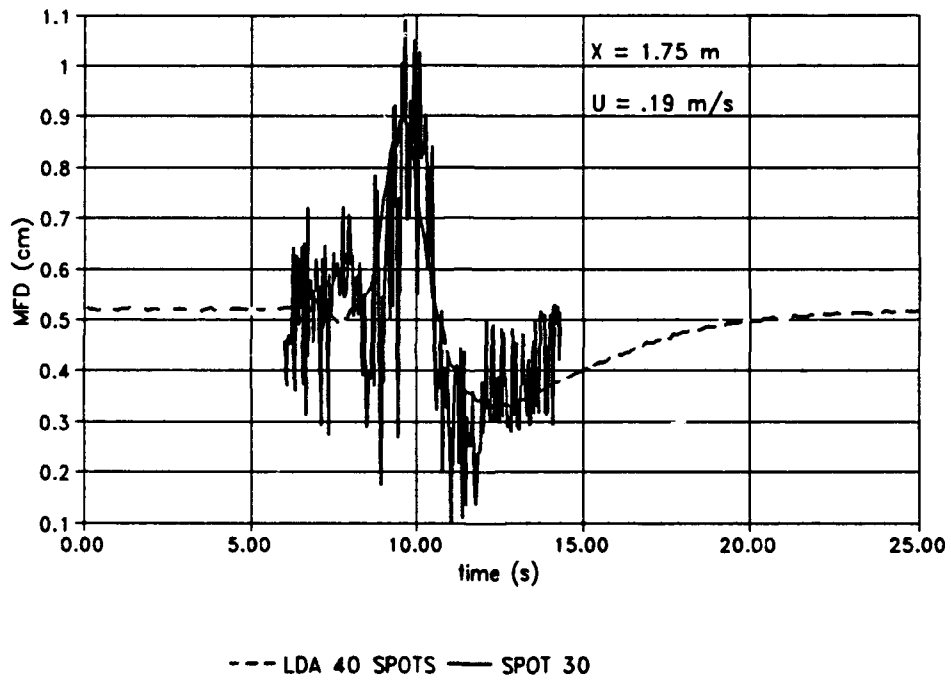


Figure 46. Hydrogen Bubble Instantaneous δ^* vs. Time Spot #30.

of ensemble averaging has a significant potential for missing strong peaks in fluctuations that could significantly modify instantaneous local momentum transfer and also noise production.

CHAPTER 4

CONCLUSIONS AND RECOMMENDATIONS

4.1. Conclusions of the Present Study

The results obtained in this study both analytically and experimentally show that the hydrogen bubble method is a valid technique for flow measurements. Although the errors were somewhat high for particular speeds or parameters, all the errors calculated are still within engineering applicability. The analytical error estimates compared reasonably well with the experimental results suggesting that the predominant sources of error have been accounted for.

The hydrogen bubble wire method showed itself to be very sensitive to the pixel resolution between timelines. It also showed that with the present electrical conditions, it is sensitive to severe gradients within the turbulent spots. The operating velocity for this apparatus was determined by the buoyancy effects for the low end and the spreading of the timelines for the high end. Both of these limitations could be stretched either way by adjusting the electrical conditions of the apparatus itself.

An analytical study using a laminar boundary layer profile substantiated the claim that the Eulerian field velocity can be represented by the Lagrangian time-averaged velocity of the bubbles. The instantaneous velocity results calculated at all velocities and time intervals yielded a maximum error of 5% in the freestream and 1% near the wall. The integral parameters showed fairly good consistency but

exhibited sensitivity to either bubble generation non-uniformity, debris in the flow, or the curve fitting procedure down by the wall, as the rms about the means was about 5-10% for a laminar boundary layer. The δ^* values in the turbulent spot passings yielded two inconsistencies with the ensemble-averaged LDA results. The hydrogen bubble method gave an opposite result to the LDA in the time shortly before the large rise in δ^* due to the large gradients in the boundary layer at this time. These gradients deformed the timeline such that the velocity profile exhibited severe deformation itself resulting in a higher value of displacement thickness. At the time of the maximum value of δ^* , the hydrogen bubble method once again yielded values substantially higher than the corresponding LDA results at this location.

The question of whether the LDA ensemble averaging scheme smears out the overall magnitude of the peaks in δ^* or whether the hydrogen bubble method accentuates the peaks due to its error band remains unanswered since a second instantaneous measurement scheme is not presently employed. Finally, a conclusion is drawn that the buoyant forces on the bubbles deep in the boundary layer were successfully handled by the implementation of a third order least-squares curve fit in this area.

4.2. Recommendations and Future Considerations

Further possible improvements in the existing equipment lie in further automation using a programmable broadcast quality video playback machine which

is exactly compatible with the frame grabber. With this piece of hardware, full automation can be achieved enabling the procedure to be that much more user effective. Also a restriction at the time of this study was the limited number of positions for placement of the wire on the test plate. A wire holder which can be placed anywhere in the test section is recommended to further increase the value of the hydrogen bubble method and take full advantage of its capabilities.

The instantaneous results for the turbulent spots may be improved by better establishing a curve fitting criteria. The present technique proved to be effective but further improvement can be made in this area. Although the reasons for the discrepancies in the hydrogen bubble and LDA δ^* averages cannot be fully explained, the potential that the error is due to averaging effects can be addressed. Since the assumption was supported on the premise that the travel distance was small and the time of travel was short, the proper adjustment would be to further reduce either of the two. In order to shorten the distance travelled either the time of travel can be decreased or the speed can be reduced.

Speeding up the pulse frequency can only be effective as long as the first timeline has fully detached from the generating wire. The speed of the freestream can also be varied through iteration. However, if any of the above change, many other parameters such as voltage, current, or pulse width must also change. In order to fully optimize the study for the turbulent case, several iterations must be performed. Full testing of any new experimental settings or image processing procedures requires full automation to fully investigate potential improvements since

processing time is presently substantial.

The hydrogen bubble wire technique is a very unique flow tool as it has many variables concerned with its operation. However, with the operating apparatus well defined and verified, there is great potential for the procedure especially for the study of unsteady flows.

REFERENCES

- Abernathy, F. H., Bertschy, J. R., Chin, R. W., "Turbulence Spectra Using Laser Doppler Anemometry and Selective Seeding," Proceedings of 5th Symposium on Turbulence 1977 (Eds. Patterson, G. K. , Zakin, J. L.) University Missouri-Rolla, 133-142.
- Asanuma, A., ed., Flow Visualization. Proceedings of the International Symposium on Flow Visualization, October 12-14, 1977 Tokyo Japan.
- Aurora Manual, Data Translation Inc., Marlboro MA 1989.
- Böttcher, J., Marschall, E., and Johnson, G., "Investigation of the Flowfield Immediately Upstream of a Hot Film Probe," Experiments in Fluids 1985 3: 215-220.
- Clutter, D. W., and Smith, A. M. O., "Flow Visualization by Electrolysis of Water," Aerospace Engineering 1961: 24-76.
- Davis, W. and Fox R. W., "An Evaluation of the Hydrogen Bubble Technique for the Quantitative Determination of Fluid Velocities Within Clear Tubes," Journal of Basic Engineering Dec. 1967: 771-776.
- Geller, E. W., An Electrochemical Method of Visualizing the Boundary Layer, Master's Thesis, Dept of Aeronautical Engineering, Mississippi State College, Aug., 1954.
- Gonzalez, R. C., and Wintz, P., Digital Image Processing 2nd Ed. Addison Wesley Publishing Co., Reading MA 1987.
- Grass, A. J., "Structural Features of Turbulent Flow Over Smooth and Rough Boundaries," Journal of Fluid Mechanics 1971 vol. 50 part 2: 233-55.
- Grob, B., Basic Television and Video Systems 5th Ed. McGraw-Hill Book Co. NY 1984.
- Hatanu, S., and Hotta, T., "Turbulence Measurements Around a Body in a Recirculating Water Channel by a Hot Film Probe," Experiments in Fluids 1983 1: 57-62.
- Hayt, W. H. Jr., Kemmerly, J. E., Engineering Circuit Analysis 4th ed. McGraw-Hill NY 1986.

- Hoffman, G. H., "The Trajectory of a Gas Bubble in an Axisymmetric Turbulent Boundary Layer," Department of the Navy, Space and Naval Warfare Systems Command Technical Memorandum, File no. 88-136, July 29, 1988.
- Kim, H. T., Kline, S. J., and Reynolds, W. C., "An Experimental Study of Turbulence Production Near a Smooth Wall in a Turbulent Boundary Layer With Zero Pressure Gradient," AFOSR Scientific Report 68-0383 Jan. 1968.
- Kim, H. T., Kline, S. J., and Reynolds, W. C., "The Production of Turbulence Near a Smooth Wall in a Turbulent Boundary Layer," Journal of Fluid Mechanics 1971 vol. 50, part 1:133-60.
- Kline, S. J., McClintock, F. A., "Describing Uncertainties in Single-Sample Experiments," Mechanical Engineering January 1953: 3-8.
- Lu, L. J., and Smith, C.R., "Image Processing of Hydrogen Bubble Flow Visualization for Determination of Turbulence Statistics and Bursting Characteristics," Experiments in Fluids 1985 3: 349-56.
- Lu, L. J., and Smith, C. R., "Image Processing of Hydrogen Bubble Flow Visualization for Quantitative Evaluation of Hairpin-Type Vortices as a Flow Structure of Turbulent Boundary Layers," Lehigh University Technical Report FM-14 1987.
- Matsui, T, Nagata, H, and Yasuda, H., "Some Remarks on Hydrogen Bubble Technique for Low Speed Water Flows," Flow Visualization, ed. A. Asanuma, 1977.
- Maxey, M. R., and Riley, J. J., "Equations of Motion for a Small Rigid Sphere in a Non-Uniform Flow," Physics of Fluids April 1983, vol. 26, no. 4: 883 - 889.
- Merzkirch, W., Flow Visualization 2nd ed. Academic Press Inc. Orlando Florida 1987.
- Milazzo, G., Electrochemistry. Theoretical Principles and Practical Applications Elsevier Pub. Co. Amsterdam 1963.
- Rasmussen, C. G., "The Air Bubble Problem in Water Flow Hot-Film Anemometry," DISA INFORMATION 1967: 21-26.
- Riley, J. J., and Gad-el-Hak, M., "The Dynamics of Turbulent Spots," in Frontiers in Fluid Mechanics (Davis, S. H., and Lumley, J. L., eds), Springer (New York) 1985: 123-155.

- Roadstrum, W. H., and Wolaver, D., Electrical Engineering for all Engineers Harper and Row Pub. NY 1987.
- Sankaran, R., Antonia, R. A., Bisset, D. K., Sokolov, M., "Flow Patterns and Organization Within Turbulent Spots," Physics of Fluids a 1991: 1560.
- Sankaran, R., Sokolov, M., and Antonia, R. A., "Substructures in a Turbulent Spot," Journal of Fluid Mechanics 1991, vol. 197: 389-414.
- Schraub, F. A., Kline, S. J., Henry, J., Runstadler, P. W., and Littell, A., "Use of Hydrogen Bubbles for Quantitative Determination of Time Dependent Velocity Fields in low Speed Water flows," Journal of Basic Engineering June 1965: 429-444.
- Schubauer, G. B., and Klebanoff, P. S., "Contributions to the Mechanics of Boundary Layer Transition," NACA TN 3489, 1955.
- Smith, C. R. and Metzler, S. P., "The Characteristics of Low Speed Streaks in the Near Wall Region of a Turbulent Boundary Layer," Journal of Fluid Mechanics 1983.
- Smith, C. R., and Paxson, R. D., "A Technique for Evaluation of Three Dimensional Behavior in Turbulent Boundary Layers Using Computer Augmented Hydrogen Bubble Wire Flow Visualization," Experimental Fluids 1983, part 1: 43-49.
- Wynanski, I., Zilberman, M., and Haritonidis, J. H., "On the Spreading of a Turbulent Spot in the Absence of a Pressure Gradient," Journal of Fluid Mechanics 1982, vol. 123: 69-90.